Medical Devices Agency of Japan (PMDA), and the Nakatani Electronic Measuring Technology Association of Japan, and by the Ministry of Education, Science, Sports and Culture, Grant-in-Aid for Young Scientists (start-up), 21890171, 2009.

References

1. Mintun M, Raichle M, Martin W, Herscovitch P. Brain oxygen utilization measured with O-15 radiotracers and positron emission tomography. J Nucl Med. 1984;25:177–87.
2. Hatazawa J, Fujita H, Kanno I, Satoh T, Iida H, Miura S, et al. Regional cerebral blood flow, blood volume, oxygen extraction fraction, and oxygen utilization rate in normal volunteers measured by the autoradiographic technique and the single breath inhalation method. Ann Nucl Med. 1995;9:15–21.
3. Shidahara M, Watabe H, Kim K, Oka H, Sago M, Hayashi T, et al. Evaluation of a commercial PET tomograph-based system for the quantitative assessment of rCBF, rOEF and rCMRO2 by using sequential administration of 15O-labeled compounds. Ann Nucl Med. 2002;16:317–27.
4. Kudomi N, Hayashi T, Teramoto N, Watabe H, Kawachi N, Ohta Y, et al. Rapid quantitative measurement of CMRO(2) and CBF by dual administration of (15)O-labeled oxygen and water during a single PET scan—a validation study and error analysis in anesthetized monkeys. J Cereb Blood Flow Metab. 2005;25:1209–24.
5. Kudomi N, Hayashi T, Watabe H, Iida H. Rapid CBF/$CMRO_2$ measurement in a single PET scan with dual tracer administration. J Cereb Blood Flow Metab. 2005;25:S672.
6. Bailey D. Transmission scanning in emission tomography. Eur J Nucl Med. 1998;25:774–87.
7. Ostertag H, Kbler W, Doll J, Lorenz W. Measured attenuation correction methods. Eur J Nucl Med. 1989;15:722–6.
8. Watabe H, Matsumoto K, Senda M, Iida HP. Performance of list mode data acquisition with ECAT EXACT HR and ECAT EXACT HR + positron emission scanners. Ann Nucl Med. 2006;20:189–94.
9. Hoffman E, Cutler P, Digby W, Mazziotta J. 3-D phantom to simulate cerebral blood flow and metabolic images for PET. IEEE Trans Nucl Sci. 1990;37:616–20.
10. Pajevic S, Daube-Witherspoon M, Bacharach S, Carson R. Noise characteristics of 3-D and 2-D PET images. IEEE Trans Med Imaging. 1998;17:9–23.
11. Kudomi N, Watabe H, Hayashi T, Iida H. Separation of input function for rapid measurement of quantitative $CMRO_2$ and CBF in a single PET scan with a dual tracer administration method. Phys Med Biol. 2007;52:1893–908.
12. Kudomi N, Choi E, Yamamoto S, Watabe H, Kim K, Shidahara M, et al. Development of a GSO detector assembly for a continuous blood sampling system. IEEE Trans Nucl Sci. 2003;50:70–3.
13. Iida H, Kanno I, Miura S, Murakami M, Takahashi K, Uemura K. Error analysis of a quantitative cerebral blood flow measurement using H2(15)O autoradiography and positron emission tomography, with respect to the dispersion of the input function. J Cereb Blood Flow Metab. 1986;6:536–45.
14. Lammertsma A, Cunningham V, Deiber M, Heather J, Bloomfield P, Nutt J, et al. Combination of dynamic and integral methods for generating reproducible functional CBF images. J Cereb Blood Flow Metab. 1990;10:675–86.
15. Iida H, Higano S, Tomura N, Shishido F, Kanno I, Miura S, et al. Evaluation of regional differences of tracer appearance time in cerebral tissues using [15O] water and dynamic positron emission tomography. J Cereb Blood Flow Metab. 1988;8:285–8.
16. Ibaraki M, Miura S, Shimosegawa E, Sugawara S, Mizuta T, Ishikawa A, et al. Quantification of cerebral blood flow and oxygen metabolism with 3-dimensional PET and 15O: validation by comparison with 2-dimensional PET. J Nucl Med. 2007;49:50–9.
17. Freedman N, Bacharach S, Carson R, Price J, Dilsizian V. Effect of smoothing during transmission processing on quantitative cardiac PET scans. J Nucl Med. 1996;37:690–4.
18. Xu M, Luk W, Cutler P, Digby W. Local threshold for segmented attenuation correction of PET imaging of the thorax. IEEE Trans Nucl Sci. 1994;41:1532–7.
19. Xu M, Cutler P, Luk W. Adaptive, segmented attenuation correction for whole-body PET imaging. IEEE Trans Nucl Sci. 1996;43:331–6.
20. Weinzapfel B, Hutchins G. Automated PET attenuation correction model for functional brain imaging. J Nucl Med. 2001;42:483–91.
21. Boellaard R, Lingen Av, Balen Sv, Lammertsma A. Optimization of attenuation correction for positron emission tomography studies of thorax and pelvis using count-based transmission scans. Phys Med Biol. 2004;49:N31–8.
22. Iwanishi K, Watabe H, Hayashi T, Miyake Y, Minato K, Iida H. Influence of residual oxygen-15-labeled carbon monoxide radioactivity on cerebral blood flow and oxygen extraction fraction in a dual-tracer autoradiographic method. Ann Nucl Med. 2009;23:363–71.
23. Gunn R, Lammertsma A, Hume S, Cunningham V. Parametric imaging of ligand receptor binding in PET using a simplified reference region model. Neuroimage. 1997;6:279–87.

Multicenter Evaluation of a Standardized Protocol for Rest and Acetazolamide Cerebral Blood Flow Assessment Using a Quantitative SPECT Reconstruction Program and Split-Dose ^{123}I-Iodoamphetamine

Hidehiro Iida[1,2], Jyoji Nakagawara[1,3], Kohei Hayashida[1,4], Kazuhito Fukushima[1,5], Hiroshi Watabe[1,2], Kazuhiro Koshino[1,2], Tsutomu Zeniya[1,2], and Stefan Eberl[1,6]

[1]Dual-Table Autoradiography SPECT Research Group in Japan, Osaka, Japan; [2]National Cerebral and Cardiovascular Center–Research Institute, Osaka, Japan; [3]Nakamura Memorial Hospital, Sapporo, Japan; [4]Takeda Hospital, Kyoto, Japan; [5]National Cerebral and Cardiovascular Center–Hospital, Osaka, Japan; and [6]Royal Prince Alfred Hospital, Sydney, Australia

SPECT can provide valuable diagnostic and treatment response information in large-scale multicenter clinical trials. However, SPECT has been limited in providing consistent quantitative functional parametric values across the centers, largely because of a lack of standardized procedures to correct for attenuation and scatter. Recently, a novel software package has been developed to reconstruct quantitative SPECT images and assess cerebral blood flow (CBF) at rest and after acetazolamide challenge from a single SPECT session. This study was aimed at validating this technique at different institutions with a variety of SPECT devices and imaging protocols. **Methods:** Twelve participating institutions obtained a series of SPECT scans on physical phantoms and clinical patients. The phantom experiments included the assessment of septal penetration for each collimator used and of the accuracy of the reconstructed images. Clinical studies were divided into 3 protocols, including intrainstitutional reproducibility, a comparison with PET, and rest–rest study consistency. The results from 46 successful studies were analyzed. **Results:** Activity concentration estimation (Bq/mL) in the reconstructed SPECT images of a uniform cylindric phantom showed an interinstitution variation of ±5.1%, with a systematic underestimation of concentration by 12.5%. CBF values were reproducible both at rest and after acetazolamide on the basis of repeated studies in the same patient (mean ± SD difference, −0.4 ± 5.2 mL/min/100 g, n = 44). CBF values were also consistent with those determined using PET (−6.1 ± 5.1 mL/min/100 g, n = 6). **Conclusion:** This study demonstrates that SPECT can quantitatively provide physiologic functional images of rest and acetazolamide challenge CBF, using a quantitative reconstruction software package.

Key Words: ^{123}I-iodoamphetamine; cerebral blood flow; acetazolamide; SPECT; vascular reactivity; quantitation

J Nucl Med 2010; 51:1624–1631
DOI: 10.2967/jnumed.110.078352

Received Apr. 27, 2010; revision accepted Jul. 14, 2010.
For correspondence or reprints contact: Hidehiro Iida, Department of Investigative Radiology, National Cerebral and Cardiovascular Center–Research Institute, 5-7-1 Suita City, Osaka 565-8565, Japan.
E-mail: iida@ri.ncvc.go.jp

Current clinical practice using SPECT relies largely on interpretation of qualitative images reflecting physiologic function. Quantitative functional parametric images may be obtained by applying mathematic modeling to SPECT data corrected for attenuation and scatter. Quantitative regional cerebral blood flow (CBF) (*1–3*) and cerebral vascular reactivity (CVR) in response to acetazolamide challenge (*4–6*) have been obtained with these techniques. One major application of such quantitative SPECT (QSPECT) approaches is the evaluation of ischemic status in patients with occlusion or stenosis in their middle cerebral arteries, to provide prognostic information of the outcome of revascularization therapies (*7*). Quantitative analysis in SPECT has also been demonstrated in the assessment of binding potential for several neuroreceptor ligands (*8,9*), for the quantitative assessment of regional myocardial perfusion (*10,11*), and for the assessment of radioaerosol deposition and clearance in healthy and diseased lungs (*12*). However, providing the standardized quantitative approach required for multicenter clinical trials has so far received only limited attention. Challenges remain in providing consistent quantitative data across institutions using a variety of SPECT equipment and vendor-specific reconstruction strategies (*13*). This limitation is attributed to a lack of standardized procedures in the reconstruction software offered by vendors, particularly in terms of correcting attenuation and scatter. Kinetic modeling for physiologic parameter estimation is also not part of the vendors' standard SPECT software. Although separate packages can be purchased for this purpose, they are not integrated and are flexible general-purpose packages, requiring considerable skill and knowledge to effectively use. Thus, they are not ideal for routine clinical use.

Scatter and attenuation occur in the object and are thus object-dependent but are not dependent on the geometry of the imaging equipment (*14*). Therefore, once a software program is developed to provide accurate image reconstruction with compensation for both attenuation and scatter, the

program should be able to provide quantitative images that are intrinsically independent of the geometric design of SPECT cameras. This is an attractive feature of SPECT for multicenter clinical studies.

From the various techniques available to correct for attenuation (*15*) and scatter (*16*), one feasible approach for clinical studies is based on a combination of attenuation correction, incorporated into the ordered-subset expectation maximization (OSEM) reconstruction (*17*), and scatter correction by the transmission-dependent convolution subtraction (TDCS) originally proposed by Meikle et al. (*18*). This approach has been extensively investigated by our group (*11,19*) for ^{99m}Tc for studies of the brain and heart (*18,20*) and also in cardiac ^{201}Tl studies (*11,21*). A recent study also demonstrated the accuracy of this approach in a combined SPECT/CT system (*22*). By incorporating a correction for collimator septal penetration by high-energy emissions, one can also make the technique applicable to ^{123}I (*19*).

The QSPECT reconstruction approach has estimated CBF images at rest in a clinical setting (*11*) and quantified CVR by measuring CBF at rest and after vasodilation in a single SPECT session. This was accomplished by using the dual-table autoradiographic (DTARG) method and a dual administration of ^{123}I-iodoamphetamine (*23*). In those studies, corrections for attenuation and scatter appeared to be essential for generating quantitative CBF maps that were consistent with those generated by ^{15}O-water PET (*11,23*).

These studies were, however, validated in a single institution using a limited range of SPECT systems, and the general applicability of this technique for different SPECT systems had yet to be fully established. Thus, the aim of this study was to verify that analysis of data with a standardized reconstruction package incorporating attenuation and scatter correction can provide reproducible results across multiple institutions for quantitative rest and acetazolamide challenge CBF estimation from a single SPECT session.

MATERIALS AND METHODS

Institutions and Subjects

The 12 participating institutions were clinical centers and generally did not have scientific staff dedicated to nuclear medicine software or hardware development. Standard, vendor-supplied software was used for the collection of the studies, with unmodified scanners and collimators clinically used for brain studies. The acquired data were reconstructed with the program package developed for this project. Manufacturers and models of camera systems and the number of detectors and collimators (including fanbeam or parallel hole) used by the institution are listed in Supplemental Table 1 (supplemental materials are available online only at http://jnm.snmjournals.org). All institutions performed experiments on physical phantoms according to the protocol described in the "Phantom Experiment" section. Of the 12 institutions, 9 obtained patient scans, whereas the remaining 3 provided only phantom data. Clinical studies were approved by institutions' ethics committees or followed guidelines for clinical research protocols authorized by the institution. All subjects at each institution gave written informed consent.

The clinical studies were divided into 3 protocols: intrainstitutional, intrasubject reproducibility (reproducibility); comparison with PET (vs. PET); and intrascan consistency of the dual-time-point split-dose (rest–rest). Studies were excluded from the analysis if there was severe patient motion during one of the studies or if there were changes in the condition of the patients between the first and second studies likely to lead to changes in CBF.

Eight institutions (institutions 1, 3, 4, 6, 8, 9, 11, and 12) participated in the reproducibility arm, in which quantitative CBF values measured on separate days were compared. In this arm, all patients experienced unilateral or bilateral stenosis or occlusion in the extracranial internal carotid artery. The patients' ages ranged from 43 to 81 y (mean ± SD, 65 ± 9 y). A total of 31 studies in this protocol were analyzed. Four patients had to be excluded from the analysis—2 because of significant changes in their pathophysiologic status between the studies and 2 because of severe motion and mispositioning in the scanner.

One institution (institution 4) performed the versus-PET studies. CBF values obtained by the DTARG method were compared with those by ^{15}O-water and PET. Studies were performed on 6 patients (5 men, 1 woman; age range, 71–74 y; mean age ± SD, 72 ± 1 y) with stenosis or occlusion of the extracranial internal carotid artery unilaterally (n = 3) or bilaterally (n = 3).

Two institutions (institutions 2 and 12) provided data for the rest–rest comparison. Five patients from institution 2 had chronic cerebral infarction, whereas 4 subjects from institution 12 had no sign of cerebral disease. Patients' ages ranged from 32 to 72 y (mean ± SD, 52 ± 15 y); 5 patients were men and 4 women.

Phantom Experiment

Three experiments were performed by each institution using the SPECT camera fitted with the collimators normally used in clinical brain studies. The first scan determined the absolute sensitivity or the becquerel calibration factor (BCF) of the reconstructed images. For 10 min, a 360° projection set was acquired of a syringe filled with a ^{123}I-iodoamphetamine solution of known radioactivity and placed at the center of the field of view. The syringe was supplied by Nihon-Medi Physics, and its radioactivity was calibrated to 111 MBq at noon on the day before the experiment, with an accuracy better than 3%, decaying to approximately 30 MBq at the time of the experiment, avoiding the dead time of the camera. The BCF was determined by dividing the absolute radioactivity by the total counts for the syringe region in the reconstructed image.

The second experiment determined the collimator septal penetration contribution (*24*) from high-energy photons into the primary 159-keV energy window for ^{123}I. A line-spread function was obtained from the projection data of a line source filled with ^{123}I-iodoamphetamine. The septal penetration was determined from the background level as described previously (*19*). A projection line-spread function was also generated from this line source placed in a water-filled cylindric phantom (diameter, 16 cm).

The third experiment used a 16-cm-diameter, 15-cm-long uniform cylindric phantom. The whole radioactivity used for the BCF determination was diluted into the phantom, and projection data were acquired for 30 min, using the clinical scan protocols described in the "Clinical Studies" section. The radioactivity concentration (counting rate per unit mass) of an approximately 0.3-mL sample from the phantom was measured using the well counters available at the various institutions. Both NaI- and plastic scintillator–based well counters were used (Supplemental Table

1). Average pixel counts derived from regions of interest on the reconstructed emission images were referred to the well counter radioactivity counting rate, to determine the cross-calibration factor between the SPECT images and well counter system. This cross-calibration factor was subsequently used for the blood sample counts of the clinical studies. Uniformity of the reconstructed emission images was evaluated.

Clinical Studies

All clinical SPECT studies followed the DTARG protocol, with dual administration of iodoamphetamine (*23*), depicted in Figure 1. Briefly, 2 dynamic scans were acquired in quick succession, with a 2-min interval between the scans. The first scan covered the initial 0- to 28-min period, and the second was acquired from 30 to 58 min. At 4 min per frame, 7 frames covered each of the 2 dynamic scan periods. ^{123}I-iodoamphetamine (111 MBq at institutions 2–12 or 167 MBq at institution 1) was infused twice over 1 min into the antecubital vein at 0 and 30 min. Acetazolamide (17 mg/kg, 1,000 mg maximum) was administered intravenously at 20 min after the first iodoamphetamine injection, corresponding to 10 min before the second iodoamphetamine injection. Projection data were summed for the acquisition duration of the first and second scans and reconstructed as described in the "QSPECT Reconstruction" section. In contrast to the study of Kim et al. (*23*), which used full arterial blood sampling, the individual arterial input functions were derived from a population-based standardized input function scaled with the whole-blood counts from a single arterial blood sample taken at approximately 10 min (*1,25–28*). This sample was also used for arterial blood gas analysis.

In the reproducibility arm, an additional, non-DTARG CBF study was performed on a separate day. Instead of DTARG, the previously reported ^{123}I-IMP autoradiographic (IMPARG) method (*1,19,25*) was performed within a month of the DTARG study. The IMPARG method is essentially equivalent to the present DTARG method, except that the IMPARG method uses a single iodoamphetamine administration to assess CBF either at rest or after acetazolamide challenge. The same image reconstruction process as for the DTARG protocol was used. In 12 studies, the DTARG protocol was used instead of IMPARG—namely, the DTARG study was performed twice to assess the CBF reproducibility at rest and after acetazolamide.

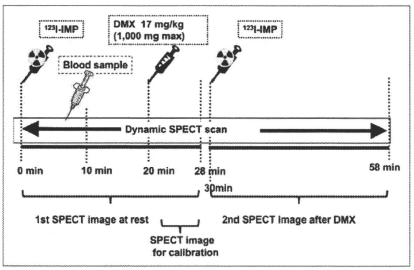

FIGURE 1. Scanning protocol flow for DTARG procedure. ^{123}I-iodoamphetamine was injected at 0 min, and 28-min resting dynamic SPECT scan was commenced. Blood sample for calibration of population input function was drawn at 10 min. Acetazolamide (DMX-diamox) was administered at 20 min. CBF values are scaled by last frame (time, 24–28 min). Second dynamic SPECT scan followed second injection of ^{123}I-iodoamphetamine at 30 min. IMP = iodoamphetamine.

In the versus-PET protocol, the PET study was performed within 2 d of the DTARG SPECT study. PET scans used intravenous ^{15}O-water both at rest and after the acetazolamide challenge. CBF images were calculated by the ^{15}O-water autoradiography technique (*29*), with careful corrections for delay and dispersion (*30–32*). Patients were stable between the SPECT and PET studies.

In the rest–rest protocol, the DTARG scan was obtained without the pharmacologic challenge during the study to evaluate the consistency of CBF values estimated from the 2 scans.

QSPECT Reconstruction

The program package for QSPECT uses a wrapper written in JAVA to run several programs written in C for Microsoft Windows systems. The package includes programs for reconstructing SPECT images, calculating functional images, coregistering images, and reslicing and printing summary logs.

The QSPECT package reconstructs images from the original projection data from commercial SPECT equipment, based on previous work by Iida and his colleagues (*19–21,23,33,34*). Reconstructed SPECT images are calibrated in Bq/mL, which provides independence from scanning parameters such as the acquisition time, number of views, matrix size, and zoom factor. Uniformity and center-of-rotation corrections and fanbeam–to–parallel beam conversion (for fanbeam collimators) were performed using the clinical routine software before reconstruction by this package.

An overall flow diagram of the correction and reconstruction process is shown in Supplemental Figure 1. The OSEM reconstruction technique includes attenuation correction (*17*). A threshold-based edge-detection algorithm generated the attenuation μ-map, assuming a uniform attenuation coefficient of 0.166 cm^{-1} for ^{99m}Tc (0.160 cm^{-1} for ^{123}I) as an average over the brain and skull (*19*). The threshold was optimized via the user interface to correctly define the brain outline. The attenuation μ-map was generated from the summed 0- to 28-min rest frame and was coregistered to the other images (*35*) reconstructed with filtered backprojection without attenuation or scatter correction. The attenuation μ-maps were forward projected to provide the transmission projection data for TDCS. The emission projections were scatter-corrected by the TDCS method, as originally proposed by Meikle et al. (*18*), and further optimized for realistic ^{99m}Tc, ^{201}Tl, and ^{123}I data in the brain and thorax regions (*20,21,23,33,34*). An offset compensated for the septal penetration of high-energy photons for ^{123}I studies, which adds fairly uniform background counts, or direct current (DC) components, to the projections.

Scatter- and attenuation-corrected images were reconstructed with OSEM (5 iterations, 5 subsets using geometric-mean projections, postreconstruction gaussian filter of 7 mm in full width at half maximum) and then realigned to the image set obtained from the first scan. The acquisition parameters and BCF were used to convert the reconstructed raw counts to Bq/mL.

The global CBF over the entire gray matter was estimated from the SPECT frame covering 24–28 min, because this timing minimizes the individual shape variations in individual input function. The look-up table generated for estimating CBF images from the complete dynamic study (0–28 min) was then

scaled to provide global cortical gray matter CBF values consistent with the 24- to 28-min frame estimates. A careful detection algorithm was used to reliably exclude extracranial accumulation of ^{123}I-iodoamphetamine (e.g., in the parotid region), which could adversely affect this scaling procedure. The regional CBF was then estimated at each pixel by means of the table look-up procedure (*25,28*). The background image at the time of the second ^{123}I-iodoamphetamine injection was estimated from the first-phase CBF images, according to the compartment model assumed in this study (*23*). An additional table look-up procedure was applied to the second dynamic dataset (30–58 min) for calculating the vasodilated (acetazolamide challenge) CBF images as described previously (*23*). The data were successfully reconstructed, and CBF was estimated at each institution. To facilitate and provide consistent analysis, the data presented are from the reanalysis conducted at the core lab (National Cerebral and Cardiovascular Center).

Data Analysis

The uniform phantom SPECT activity estimates were compared with the known activity in the phantom. Images for the baseline study were displayed with subsequent images using an absolute flow value scale to visually ascertain regional and global differences in flow. Regions of interest were placed on the middle cerebral artery territories of both hemispheres, and the average flow values between the different methods were compared and plotted. Bland–Altman plots and the SD of the differences evaluated the consistency of CBF values obtained from the reproducibility and versus-PET protocols.

All data were presented as mean ± SD. Pearson correlation analysis and linear regression analysis were used to evaluate relationships between the 2 CBF values. A P value less than 0.05 was considered statistically significant.

RESULTS

Phantom Studies

In the 16-cm scattering cylinder line source experiment, the scatter-uncorrected images show background counts extending beyond the phantom, from septal penetration of the high-energy photons. The scatter correction is largely effective in correcting for scatter and septal penetration counts. As shown in Supplemental Figure 2, the Toshiba-ECAM low- to medium-energy general-purpose (LMEGP) collimator, designed for reduced ^{123}I septal penetration, compared with the standard low-energy high-resolution collimator (GE Healthcare), demonstrates reduced scatter and septal penetration counts. The lower septal penetration of the Toshiba-ECAM LMEGP collimators is also supported by a lowered scatter correction offset value (DC = 0.05, compared with DC = 0.20 for the GE low-energy high-resolution collimator). The reduced scatter and septal penetration result in more complete removal of scatter for the LMEGP collimator.

Figure 2 displays reconstructed slices of the uniform phantom for all 12 institutions, scaled to the same maximum activity concentration. The estimated activity concentrations from these studies, compared with the known activity concentration, represented an accuracy of 87.5% ± 5.1% (Supplemental Table 1). The well counter–to–SPECT cross-calibration factor, which represents the sensitivity of the well counter system for ^{123}I, was 0.5–1.0 for NaI systems and 0.1–0.2 for plastic scintillation detector systems. The BCF values were consistent for the same SPECT camera–collimator configurations.

Clinical Studies

Figure 3A shows typical CBF images obtained at 4 institutions with 4 different γ-camera vendors, performed as part of the reproducibility arm of the study. Each case shows different CBF distributions both at rest and after acetazolamide challenge. The acetazolamide images obtained using the DTARG method agree well with the images subsequently obtained with the IMPARG method after acetazolamide infusion.

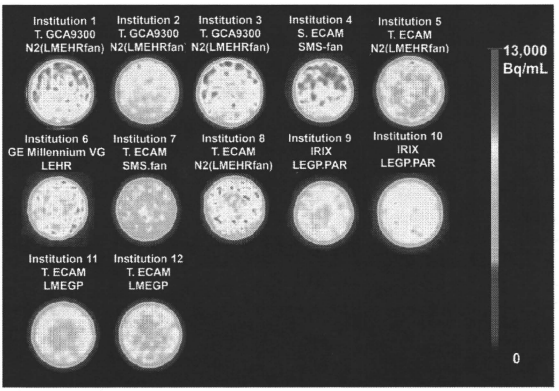

FIGURE 2. Reconstructed slices through uniform phantom from the participating 12 institutions. Experiment was designed to have same phantom activity concentration for each center's study. Nonuniformities and also differences in absolute activity concentration estimates can be observed, highlighting need for rigorous calibration, flood correction, and quality control. Legend above each image gives institution number (given in Supplemental Table 1), γ-camera model, and collimator used.

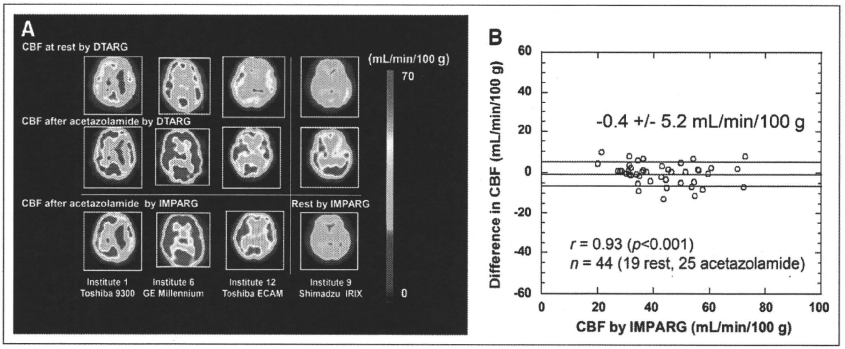

FIGURE 3. (A) Images from reproducibility study. CBF images obtained at rest and after acetazolamide with DTARG method. Repeated scan (third row) within 1 mo using IMPARG method and acetazolamide stress (columns 1–3) and at rest (last column). Images demonstrate that CVR can be estimated with this technique and demonstrate good reproducibility of measuring both at rest and after acetazolamide challenge CBF. (B) Bland–Altman plot showing difference vs. IMPARG CBF values estimated from DTARG method and repeated IMPARG studies to assess reproducibility. Little systematic bias is detected (mean difference, −0.4 mL/100 g/min), and SD of differences is moderate (5.2 mL/100 g/min). Correlation coefficient of $r = 0.93$ ($P < 0.001$) was found.

CBF images of a subject with left middle cerebral artery occlusion are shown in Supplemental Figure 3 for slices covering the whole brain. The images demonstrate reduced CBF after acetazolamide challenge in the left middle cerebral artery territory. The good reproducibility is confirmed by the Bland–Altman plot comparison of DTARG CBF values, with the CBF values obtained at a different imaging session with IMPARG or DTARG (Fig. 3B). The SD of the differences is 5.2 mL/100 g/min, with low bias supported by the mean difference of 0.4 mL/100 g/min. Regression analysis between DTARG and IMPARG values yielded a significant correlation ($P < 0.001$), with a correlation coefficient of $r = 0.93$.

Figure 4A shows MR and CBF images at rest and after acetazolamine obtained with DTARG SPECT and ^{15}O-water PET in a 73-y-old male patient (63 kg) with right internal carotid artery occlusion and left internal carotid stenosis. The MR images do not show any evidence of cerebral infarction in either hemisphere. Rest CBF was reduced bilaterally in the frontal-to-parietal regions, and acetazolamide increased CBF in left parietal regions but not in the right parietal area. DTARG CBF indicated the loss of vasoreactivity in the right internal carotid artery stenotic area. These findings were consistent with those from the PET evaluation. An additional example is shown in Supplemental Figure 4 for a 74-y-old female patient (48 kg) with left internal carotid artery stenosis, for whom MR images did not show cerebral infarction. DTARG CBF demonstrated preserved CBF in both hemispheres but reduced CBF reactivity in the left middle cerebral artery territory. The findings were again consistent with those from PET. Figure 4B compares the flow values obtained at rest and after acetazolamide with DTARG with the corresponding values obtained by ^{15}O-water PET. The SD of the differences is 5.1 mL/100 g/min, with the significant underestimation by ^{15}O-water PET, compared with PET by the DTARG method, highlighted by a mean difference of −6.1 mL/100 g/min. The Pearson analysis showed a significant correlation ($P < 0.001$), with a correlation coefficient of $r = 0.88$.

The results from the rest–rest protocol are summarized in Figure 5. The differences between the measurements performed with the 2 injections were small, with good agreement between the 2 flow values. The mean ± SD of the differences was 0.6 ± 2.9 mL/100 g/min.

DISCUSSION

The QSPECT package provided quantitative images consistent between the participating centers, using dual- or triple-detector SPECT scanners and collimators routinely used for nonquantitative brain studies. All centers successfully acquired the dynamic SPECT images, and the data from the variety of cameras encountered were successfully processed by the software package. Rest CBF and CVR could be readily obtained by the participating institutions in a single, clinically practical, 1-h scanning session. Good reproducibility of CBF estimates was observed in 31 pairs of studies at 8 institutions (Fig. 3), and the CBF estimated with the ^{123}I-iodoamphetamine SPECT agreed well with ^{15}O-water PET CBF at 1 institution (Fig. 4). The CBF values after the second injection of the DTARG were consistent with the values obtained after the

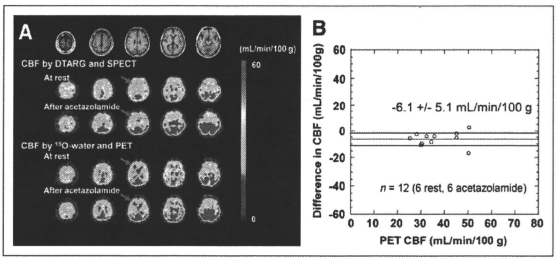

FIGURE 4. (A) MR and CBF images at rest and after acetazolamide stress assessed with corresponding measurements with ^{15}O-water PET (vs. PET evaluation) in patient with right internal carotid artery occlusion and left internal carotid stenosis. Gaussian filter was not applied to SPECT CBF in this display. (B) Bland–Altman plot. Moderate underestimation of CBF determined by DTARG method, compared with PET, is observed (mean difference, −6.1 mL/100 g/min). Correlation coefficient of $r = 0.88$ ($P < 0.001$) was found.

first injection when no vasodilating stress was given in 9 studies at 2 institutions (Fig. 5).

Quantitative CBF and CVR in response to acetazolamide challenge can be of significant prognostic value for patients considered for revascularization of cerebral arteries (*5–7*). The previously validated IMPARG method requires 2 independent scans on different days to assess the CVR (*5–7*), limiting it for routine clinical studies. The DTARG protocol to quantitatively assess CBF both at rest and after acetazolamide from a single dynamic SPECT session with the dual administration of ^{123}I-iodoamphetamine (*23*) facilitates clinical use. Errors caused by ambiguity in the absolute scaling, and possible changes in physiologic status of the subjects between scans, can be reduced substantially with the DTARG protocol. The quantitative reconstruction program enabled the compartment model–based kinetic analysis to compensate for the residual radioactivity concentration during the second session of the dynamic scan.

Major error sources in SPECT, namely attenuation and scatter, are only object-dependent (*14*) and not γ-camera– or collimator-dependent, and thus SPECT images obtained by this quantitative reconstruction package should be consistent across systems. Septal penetration of high-energy photons for ^{123}I is, however, collimator-dependent (*24*) but could be compensated as part of the TDCS scatter correction algorithm (*11*), as demonstrated in Supplemental Figure 2. The radioactivity concentration of the uniform cylinder phantom estimated in units of Bq/mL was consistent and showed variation within ±5.1% (Fig. 2; Supplemental Table 1), though a systematic underestimation by 12.5%, which is attributed to the BCFs being derived from a line source in air, reconstructed without scatter, attenuation, and septal penetration corrections. However, this underestimation does not affect the CBF estimation, because it relies on the direct cross-calibration between the γ-counter used to count the blood sample and the SPECT measurements.

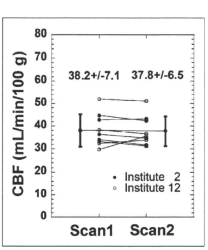

FIGURE 5. Results from rest–rest evaluation carried out at 2 institutions (2 and 12). In this study, DTARG method was performed as per normal protocol but without pharmacologic stress. CBFs estimated with first injection (left on graph) are in good agreement with those estimated after second injection (right on graph).

This phantom study also highlighted the importance of proper calibration and quality control of the γ-camera to avoid artifacts and bias in the reconstructed images. These corrections were applied, as for other clinical studies, by the vendors' software rather than as part of the QSPECT system, because these corrections are typically performed online and on-the-fly, with only the corrected data being stored. The nonuniformities seen on some phantom images should improve with more rigorous quality-control procedures.

The previously validated population-based input function requiring only a single arterial blood sample for scaling (*1,25–28*) has been incorporated in the software package. Blood from this single arterial sample is also used to measure arterial blood gases, which are relevant and of interest clinically in these patients. The timing of the single blood sample (~10 min after iodoamphetamine injection) was optimized previously (*1,25–28*) to minimize the errors associated with individual differences in shape of the arterial input function. In addition, absolute global CBF was estimated from SPECT images taken at an optimized mid scan time of approximately 30 min (24–28 min), rather than from the initial part of the study, to maximize the accuracy of using the population-based input function (*1,25–28*).

Partial-volume correction has not been implemented as part of this processing protocol. Partial-volume effects can potentially lead to underestimation of flow values in gray matter regions because of the limited resolution of SPECT. The small underestimation of 6.1 mL/100 g/min by the DTARG method, compared with ^{15}O-water PET (Fig. 4B), is attributed to the partial-volume effects due to differences in resolution between PET and SPECT. The underestimation can also lead to variations in CBF values obtained with different-

resolution collimators. However, consistent postreconstruction filtering, as applied in this study, can reduce this effect.

Only the reproducibility within an institution was assessed. Hence, the reproducibility of measurements between institutions cannot be gleaned from these data, particularly because patients with vascular disease were studied. Thus, unlike estimates from healthy volunteers, flow values and vascular reactivity are expected to vary from patient to patient, and flow values determined at one institution with one group of patients are therefore not directly comparable with flow values from another group of patients in another institution. A realistic brain phantom, such as recently developed by our group, simulating head contour with bone attenuation, could be used to assess the consistency of brain images between institutions.

CONCLUSION

The developed QSPECT package allows absolute CBF and CVR to be estimated in routine clinical studies. This multicenter study has demonstrated the applicability of QSPECT for a variety of clinical settings and equipment. Results from the studies suggest that a change of approximately 10% or 5 mL/min/100 g can be readily detected in follow-up studies. The graphical user interface for easily controlling the in-built sophisticated programs and tools ensures that routine use does not require dedicated support from scientific or computing staff. The package is now successfully used in over 130 institutions in Japan, and more than 25,000 patient studies have been analyzed with the QSPECT package.

ACKNOWLEDGMENTS

We thank the staff of each of the following institutions that participated in this project for their invaluable help with supporting the SPECT studies: Azabu Neurosurgical Hospital, Sapporo City; Asahikawa Red Cross Hospital, Asahikawa City; Handa City Hospital, Handa City; Ichinomiya Municipal Hospital, Ichinomiya City; Kashiwaba Neurosurgical Hospital, Sapporo City; Japanese Red Cross Kobe Hospital, Kobe City; Nakamura Memorial Hospital, Sapporo City; National Cardiovascular Center, Osaka; Ogori Daiichi General Hospital, Yamaguchi City; Oji General Hospital, Tomakomai City; Sunagawa City Medical Center, Sunagawa City; and Teine Keijinkai Hospital, Sapporo City. The present study was supported by the Japan Cardiovascular Research Foundation and a grant for Translational Research from the Ministry of Health, Labor and Welfare (MHLW), Japan.

REFERENCES

1. Iida H, Akutsu T, Endo K, et al. A multicenter validation of regional cerebral blood flow quantitation using [^{123}I]iodoamphetamine and single photon emission computed tomography. *J Cereb Blood Flow Metab.* 1996;16:781–793.
2. Hatazawa J, Iida H, Shimosegawa E, Sato T, Murakami M, Miura Y. Regional cerebral blood flow measurement with iodine-123-IMP autoradiography: normal values, reproducibility and sensitivity to hypoperfusion. *J Nucl Med.* 1997;38:1102–1108.
3. Yamaguchi T, Kanno I, Uemura K, et al. Reduction in regional cerebral metabolic rate of oxygen during human aging. *Stroke.* 1986;17:1220–1228.
4. Ogasawara K, Ito H, Sasoh M, et al. Quantitative measurement of regional cerebrovascular reactivity to acetazolamide using ^{123}I-*N*-isopropyl-*p*-iodoamphetamine autoradiography with SPECT: validation study using $H_2{}^{15}O$ with PET. *J Nucl Med.* 2003;44:520–525.
5. Ogasawara K, Ogawa A, Terasaki K, Shimizu H, Tominaga T, Yoshimoto T. Use of cerebrovascular reactivity in patients with symptomatic major cerebral artery occlusion to predict 5-year outcome: comparison of xenon-133 and iodine-123-IMP single-photon emission computed tomography. *J Cereb Blood Flow Metab.* 2002;22:1142–1148.
6. Ogasawara K, Ogawa A, Yoshimoto T. Cerebrovascular reactivity to acetazolamide and outcome in patients with symptomatic internal carotid or middle cerebral artery occlusion: a xenon-133 single-photon emission computed tomography study. *Stroke.* 2002;33:1857–1862.
7. Ogasawara K, Ogawa A. JET study (Japanese EC-IC Bypass Trial) [in Japanese]. *Nippon Rinsho.* 2006;64(suppl 7):524–527.
8. Fujita M, Ichise M, Zoghbi SS, et al. Widespread decrease of nicotinic acetylcholine receptors in Parkinson's disease. *Ann Neurol.* 2006;59:174–177.
9. Deloar HM, Watabe H, Kudomi N, Kim KM, Aoi T, Iida H. Dependency of energy and spatial distributions of photons on edge of object in brain SPECT. *Ann Nucl Med.* 2003;17:99–106.
10. Iida H, Eberl S, Kim KM, et al. Absolute quantitation of myocardial blood flow with ^{201}Tl and dynamic SPECT in canine: optimisation and validation of kinetic modelling. *Eur J Nucl Med Mol Imaging.* 2008;35:896–905.
11. Iida H, Eberl S. Quantitative assessment of regional myocardial blood flow with thallium-201 and SPECT. *J Nucl Cardiol.* 1998;5:313–331.
12. Eberl S, Chan HK, Daviskas E, Constable C, Young I. Aerosol deposition and clearance measurement: a novel technique using dynamic SPET. *Eur J Nucl Med.* 2001;28:1365–1372.
13. Hapdey S, Soret M, Ferrer L. Quantification in SPECT: myth or reality? A multicentric study. *IEEE Nucl Sci Symp Conf Rec.* 2004;5:3170–3317.
14. Graham LS, Fahey FH, Madsen MT, van Aswegen A, Yester MV. Quantitation of SPECT performance: report of Task Group 4, Nuclear Medicine Committee. *Med Phys.* 1995;22:401–409.
15. Hendel RC, Corbett JR, Cullom SJ, DePuey EG, Garcia EV, Bateman TM. The value and practice of attenuation correction for myocardial perfusion SPECT imaging: a joint position statement from the American Society of Nuclear Cardiology and the Society of Nuclear Medicine. *J Nucl Cardiol.* 2002;9:135–143.
16. Zaidi H, Koral KF. Scatter modelling and compensation in emission tomography. *Eur J Nucl Med Mol Imaging.* 2004;31:761–782.
17. Hudson HM, Larkin RS. Accelerated image reconstruction using ordered subsets of projection data. *IEEE Trans Med Imaging.* 1994;13:601–609.
18. Meikle SR, Hutton BF, Bailey DL. A transmission-dependent method for scatter correction in SPECT. *J Nucl Med.* 1994;35:360–367.
19. Iida H, Narita Y, Kado H, et al. Effects of scatter and attenuation correction on quantitative assessment of regional cerebral blood flow with SPECT. *J Nucl Med.* 1998;39:181–189.
20. Narita Y, Eberl S, Iida H, et al. Monte Carlo and experimental evaluation of accuracy and noise properties of two scatter correction methods for SPECT. *Phys Med Biol.* 1996;41:2481–2496.
21. Narita Y, Iida H, Eberl S, Nakamura T. Monte Carlo evaluation of accuracy and noise properties of two scatter correction methods for ^{201}Tl cardiac SPECT. *IEEE Trans Nucl Sci.* 1997;44:2465–2472.
22. Willowson K, Bailey DL, Baldock C. Quantitative SPECT reconstruction using CT-derived corrections. *Phys Med Biol.* 2008;53:3099–3112.
23. Kim K, Watabe H, Hayashi T, et al. Quantitative mapping of basal and vasareactive cerebral blood flow using split-dose ^{123}I-idoamphetamine and single photon emission computed tomography. *Neuroimage.* 2006;33:1126–1135.
24. Kim KM, Watabe H, Shidahara M, Ishida Y, Iida H. SPECT collimator dependency of scatter and validation of transmission dependent scatter compensation methodologies. *IEEE Trans Nucl Sci.* 2001;48:689–696.
25. Iida H, Itoh H, Nakazawa M, et al. Quantitative mapping of regional cerebral blood flow using iodine-123-IMP and SPECT. *J Nucl Med.* 1994;35:2019–2030.
26. Iida H, Nakazawa M, Uemura K. Quantitation of regional cerebral blood flow using 123I-IMP from a single SPECT scan and a single blood sampling: analysis on statistical error source and optimal scan time [in Japanese]. *Kaku Igaku.* 1995;32:263–270.
27. Kurisu R, Ogura T, Takikawa S, Saito H, Nakazawa M, Iida H. Estimation and optimization of the use of standard arterial input function for split-dose administration of *N*-isopropyl-*p*[^{123}I]iodoamphetamine [in Japanese]. *Kaku Igaku.* 2002;39:13–20.

28. Ogura T, Takikawa S, Saito H, Nakazawa M, Shidahara M, Iida H. Validation and optimization of the use of standardized arterial input function in *N*-isopropyl-*p*[^{123}I]iodoamphetamine cerebral blood flow SPECT [in Japanese]. *Kaku Igaku.* 1999;36:879–890.
29. Shidahara M, Watabe H, Kim KM, et al. Evaluation of a commercial PET tomograph-based system for the quantitative assessment of rCBF, rOEF and $rCMRO_2$ by using sequential administration of ^{15}O-labeled compounds. *Ann Nucl Med.* 2002;16:317–327.
30. Iida H, Higano S, Tomura N, et al. Evaluation of regional differences of tracer appearance time in cerebral tissues using [^{15}O] water and dynamic positron emission tomography. *J Cereb Blood Flow Metab.* 1988;8:285–288.
31. Iida H, Kanno I, Miura S, Murakami M, Takahashi K, Uemura K. Error analysis of a quantitative cerebral blood flow measurement using $H_2{}^{15}O$ autoradiography and positron emission tomography, with respect to the dispersion of the input function. *J Cereb Blood Flow Metab.* 1986;6:536–545.
32. Iida H, Kanno I, Miura S, Murakami M, Takahashi K, Uemura K. A determination of the regional brain/blood partition coefficient of water using dynamic positron emission tomography. *J Cereb Blood Flow Metab.* 1989;9:874–885.
33. Iida H, Shoji Y, Sugawara S, et al. Design and experimental validation of a quantitative myocardial ^{201}Tl SPECT System. *IEEE Trans Nucl Sci.* 1999;46:720–726.
34. Narita Y, Iida H. Scatter correction in myocardial thallium SPECT: needs for optimization of energy window settings in the energy window-based scatter correction techniques [in Japanese]. *Kaku Igaku.* 1999;36:83–90.
35. Eberl S, Kanno I, Fulton RR, Ryan A, Hutton BF, Fulham MJ. Automated interstudy image registration technique for SPECT and PET. *J Nucl Med.* 1996;37:137–145.

Full Paper

CONTRAST MEDIA & MOLECULAR IMAGING

Received: 11 August 2009, Revised: 1 April 2010, Accepted: 8 April 2010, Published online in Wiley Online Library: 27 May 2010

(wileyonlinelibrary.com) DOI:10.1002/cmmi.389

Design and characterization of a polymeric MRI contrast agent based on PVA for *in vivo* living-cell tracking

Yoichi Tachibana[a], Jun-ichiro Enmi[b], Atsushi Mahara[a], Hidehiro Iida[b] and Tetsuji Yamaoka[a]*

A novel water-soluble MRI contrast agent for *in vivo* living cell tracking was developed. Unlike the conventional *in vivo* cell tracking system based on superparamagnetic iron oxide beads, the newly developed contrast agent is eliminated from the body when the contrast agent exits the cells upon cell death, which makes living cell tracking possible. The contrast agent is composed of gadolinium chelates (Gd–DOTA) and a water-soluble carrier, poly(vinyl alcohol) (PVA), which is known to interact with cells and tissues very weakly. Since the Gd–PVA was not taken up by cells spontaneously, the electroporation method was used for cell labeling. The delivered Gd–PVA was localized only in the cytosolic compartment of growing cells with low cytotoxicity and did not leak out of the living cells for long periods of time. This stability may be due to the weak cell-membrane affinity of Gd–PVA, and did not affect cell proliferation at all. After cell labeling, signal enhancement of cells was observed *in vitro* and *in vivo*. These results indicate that Gd–PVA can visualize only the living cells *in vivo* for a long period of time, even in areas deep within large animal bodies. Copyright © 2010 John Wiley & Sons, Ltd.

Keywords: MRI; cell tracking; intracellular delivery; cell transplantation; Gd chelate

1. INTRODUCTION

Over the past decade, there has been increasing interest in developing cell transplantation therapy (1–3) for various diseases such as ischemic limbs (4), infarcted myocardium (5,6) and diabetic retinopathy (7). In particular, the transplantation of autologous cells such as bone marrow- or fat tissue-derived mesenchymal stem cells is much safer than heterologous transplantation in terms of rejection, and is promising in clinical use. However, the mechanism of cell transplantation therapy remains a matter of debate. One possible mechanism is the differentiation of transplanted cells into functional cells, and another is the paracrine effect due to the produced cytokines (8). Moreover, even the engraftment ratio and survival period of the transplanted cells remain unclear. A general method of analyzing the transplanted cells, such as immunostaining, cannot be used for autologous cell transplantation because there is no phenotypic difference between transplanted cells and host cells. In recent years, then, noninvasive tracking systems for cell transplantation are attracting a great deal of attention (9,10).

Optical imaging methods using fluorescence- or bioluminescence-labeled cells have been studied extensively (11,12). Recently, green fluorescent protein (GFP)-transgenic animal or GFP-positive cells have become widely available and have been easily analyzed using various *in vivo* optical imaging instruments. However, since optical lights can penetrate tissues less than 10 mm in the case of fluorescence and 30 mm in the case of bioluminescence, only mice or rats can be used in this system (13). Therefore, cell transplantation model systems cannot be used for various diseases in large animals (14–16). In addition, the resolution is low, and the transplanted cells can be detected as large circles in small animals (13).

In contrast, magnetic resonance imaging (MRI) is a more promising system because of its high resolution, its absence of limitations on animal size and its noninvasiveness. In order to detect the transplanted cells in host tissues using MRI, cells should be labeled with contrast agents. In the past 15 years, superparamagnetic iron oxide particles (SPIO) have been studied as a means of labeling cells because of their high sensitivity (17,18). SPIO are superior to other contrast agents in terms of the detection of cells. Rice *et al.* reported the homing phenomena of adipose-derived stem cells in cerebral infarction (19). Stuckey *et al.* reported the monitoring of bone marrow stromal cells in the infarcted heart (20). Targeted cells were usually labeled with SPIO by the endocytosis mechanism or by using gene-transfection agents. However, in long-term tracking of cells, one of the problems with this system is the fate of SPIO which leaks out of

* *Correspondence to: T. Yamaoka, Department of Biomedical Engineering,Advanced Medical Engineering Center, National Cardiovascular Center Research Institute, Suita 565-8565, Japan.*
E-mail: yamtet@ri.ncvc.go.jp

a *Y. Tachibana, A. Mahara, T. Yamaoka*
Department of Biomedical Engineering,Advanced Medical Engineering Center, National Cardiovascular Center Research Institute, Suita 565-8565, Japan

b *J.-i. Enmi, H. Iida*
Department of Investigative Radiology,Advanced Medical Engineering Center, National Cardiovascular Center Research Institute, Suita 565-8565, Japan

Contract/grant sponsor: Ministry of Health, Labour and Welfare of Japan (Health and Labour Sciences Research Grants, Research on Nanotechnical Medical).
Contract/grant sponsor: Research Grant for Cardiovascular Diseases, Ministry of Health, Labour and Welfare of Japan; contract/grant number: 18A-2.

cells (free SPIO) due to exocytosis or cell death. Additionally, SPIO that has undergone intracellular uptake is slowly digested, releasing its iron. The free SPIO remains in the body and continues to show MR contrast, creating the potential for misunderstanding (21). Amsalem *et al.* reported that the observed MRI signals after transplantation of SPIO-labeled MSCs were not attributed to transplanted cells but to cardiac macrophages which took up the released SPIO from transplanted cells (22). Li *et al.* reported that SPIO undergoing cell death was internalized by macrophages or remained in the local tissue (23).

The most important part of cell tracking is to track only the living cells. In the present study, a novel water-soluble contrast agent was designed and an effective intracellular delivery system was established. Gd–DOTA (1,4,7,10-tetraazacyclo-dodecane-*N,N',N'',N'''*- tetraacetic acid) was conjugated to a bioinert and highly water-soluble polymeric carrier, poly(vinyl alcohol) (PVA). PVA is known to circulate for a long period of time in the blood stream *in vivo* because of its very weak interaction with the blood cells, macrophages or tissues. It was reported that the amount of PVA ingested by macrophages was much less than that of bovine serum albumin (24). The conjugates would be expected to be eliminated from the tissues without being ingested by macrophages when they are outside of the dead cells. The intracellular delivery system of the conjugates was established using an electroporation system, and the cytotoxicity, intracellular stability, body distribution and MR-imaging ability of the contrast agent were studied *in vitro* and *in vivo*.

2. RESULTS

2.1. Synthesis of Gd–PVA (*4a–d*)

Conjugates **4a–d** were synthesized in three steps using PVA with a molecular weight of 74 800 (**1**) as shown in Scheme 1.

The structure of conjugates **4a–d** was confirmed by ^{1}H-NMR spectroscopy and their characteristics are summarized in Table 1. At step 1, the introduction ratios of diamine ($m/n \times 100$ in Scheme 1) were 13.2, 7.5, 3.6 and 12.9%, respectively. At step 2, DOTA-NHS-ester was completely reacted with free NH_2 groups on **2** because the peak of 2.79 ppm had disappeared. These polymers were soluble in water and DMSO and insoluble in acetone, toluene and tetrahydrofuran. The Gd (III) content of the conjugates (**4a–d**) was analyzed by inductively coupled plasma atomic emission spectroscopy. To observe the cell labeling efficiency and the intracellular distribution of the conjugates, Gd–PVA labeled with fluorescence (**4d**) was synthesized. MR imaging of labeled cells was carried out after confirming the cell uptake of **4d** with fluorescent microscopy. By contrast, the cytotoxicity assay was performed using **4b** without FITC because the wavelength of FITC overlapped with that of the WST assay.

The increase of the relaxivities (R_1) of **4a–d** with the increased introduction ratio of DOTA may be due to an increased rotational correlation and constructive restriction of motion. A maximum reflexivity value of 7.1 mM^{-1} s^{-1} was observed at 13.2 mol% (**4a**). All of the relaxivities of **4a–d** were higher than that of clinically used Gd–DTPA (5.1 mM^{-1} s^{-1}), suggesting that each conjugate can be used as an effective contrast agent.

2.2. *In vitro* T_1-weighted MR measurements of polymer solutions

Figure 1 shows the MR images of **4d** solutions with different concentrations at 4.7 T. The T_1-weighted MRI signal of the **4d** solution increased with the increased polymer unit concentration. Significant contrast enhancement was seen over 0.2 mM. To achieve cell imaging, it is necessary to introduce the contrast agents at sufficient concentrations in the cells.

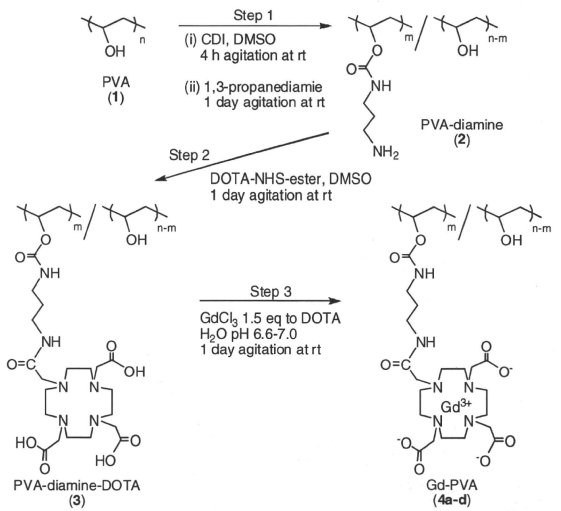

Scheme 1.

Table 1. Synthesis of **4a–d** with different contents of gadolinium chelates

	Introduction ratio of DOTA[a] (mol%)	Mn[b] ($\times 10^5$)	M_w/M_n[b]	Gd[c] (wt%)	Gd/DOTA (mol%)	FITC label	R_1 (mM^{-1} s^{-1})
4a	13.2	1.6	1.1	12.0	70.0	–	7.1
4b	7.5	1.1	1.2	9.2	69.1	–	6.2
4c	3.6	1.2	1.2	5.8	67.0	–	6.2
4d	12.9	—	—	9.3	53.9	+	7.0

[a]Scheme 1, $m/n \times 100$.
[b]Determined by size exclusion chromatography using 0.25 mM phosphate buffer as eluent with polystyrene standards.
[c]Determined by inductively coupled plasma atomic emission spectroscopy measurement.

2.3. Cytotoxicity of Gd–PVA to NIH-3T3 cells and cell labeling by electroporation

Gd–PVA **4b** was used for a cytotoxicity assay since FITC introduced to **4d** obstructs the accurate WST-1 assay. The viability of NIH-3T3 cells in the presence of **4b** was not affected even at high concentrations (10 mM; polymer unit concentration in culture medium) for up to 3 days (see Supplementary Information). The low affinity of PVA (24) might suppress the interaction of Gd–PVA with the cell membrane and decrease the cytotoxicity. In fact, weak interaction was demonstrated by a simple experiment as follows. Compound **4d** was added to the culture medium of NIH-3T3 cells, and the cells were incubated for 1 h. After washing with PBS three times, no fluorescence induced by **4d** was observed, indicating that **4d** was unable to attach to the cell membrane or enter the cells spontaneously.

To deliver such a bio-inert substance into cells, we selected an electroporation method that is mainly used to transfect DNA into cells. Since this method can introduce a large amount of polymeric substances into any kind of cells nonspecifically with low cytotoxicity, it is suitable for labeling various cells including established cell lines, somatic stem cells, or even embryonic stem cells for cell transplantation (25,26). When electroporation was carried out, the concentration of Gd–PVA in culture medium was set to 10 mM (polymer unit concentration) based on the result of the cytotoxicity assay.

Figure 2 shows bright field and fluorescent photomicrographs of NIH-3T3 cells 3 days after electroporation with **4d**. Almost all cells were labeled efficiently, and the intracellular **4d** was interestingly located only in the cytosolic compartment of NIH-3T3 cells even after cell proliferation. This intracellular distribution pattern is different from that for endocytosis, which is made from bright dots.

The stability of Gd–PVA in NIH-3T3 cells was assessed by measuring the total fluorescence intensity of the growing NIH-3T3 cells with time. The number of Gd(III) molecules in one cell calculated from the fluorescence intensity was 7.3×10^8 per cell just after electroporation. Cells were cultured for a given period of time without subculture and then lysed. Before the cells were lysed, they were washed by PBS sufficiently to eliminate any **4d** leaching from them. Figure 3 represents the total fluorescence intensity of **4d** in NIH-3T3 cells (solid circle) and cellular proliferation rates (open circle). Fluorescence derived from **4d** in cells showed no significant change over 10 days, and the labeled cells grew well. These results show that **4d** can remain in the cytosolic compartment stably for a long period of time without having any effect on cell proliferation.

2.4. *In vitro* T_1-weighted MR measurements of the labeled NIH-3T3

Figure 4a shows an MR image of the NIH-3T3 cell suspensions at 4.7 T. Compound **4d**-labeled NIH-3T3 cell suspension, non-labeled NIH-3T3 cell suspension and cell-free and Gd-free medium were left at rest for 1 day to allow the cells to be precipitated to the bottom of the test tube. Clear signal enhancement in tube 1 at slice B passing through the precipitated cells was seen. On the other hand, no signal was observed in tube 1 at slice A, which indicates that **4d** did not leak out of the cells and that **4d** in cells gives sufficient MR contrast irrespective of the small amount of free water in the cells

To examine the cell density dependence of signal enhancement, we next acquired MR images of **4d**-labeled NIH-3T3 cells at different densities in agarose gel, which was used to fix the transplanted cells in the experiment involving the injection of cells into a rat (Fig. 4b). MRI can depict at least 3.5×10^6 NIH-3T3

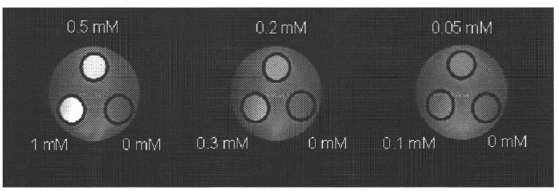

Figure 1. *In vitro* T_1-weighted MR measurements of **4d** in water at 4.7 T at the concentrations of 0, 0,05, 0.1, 0.2, 0.3, 0.5, and 1.0 mM. Three test tubes containing different concentrations were fixed vertically. A horizontal section was scanned. These images were acquired using a 2 D spin echo sequence with a TR of 2000 ms and a TE of 16 ms. These images were displayed using the same window level and window width.

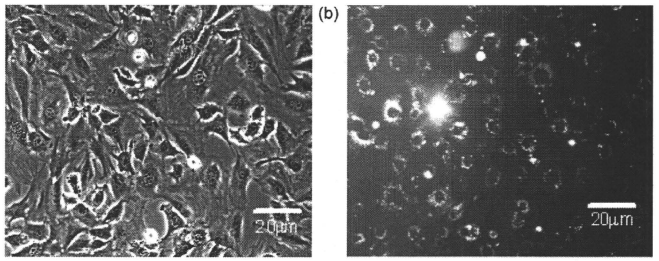

Figure 2. (a) Phase image and (b) fluorescent image of NIH-3T3 cells labeled with **4d** (FITC-Gd-PVA) at 3 days after electroporation. After electroporation, cells were washed three times by PBS. The bright ring forms showed cytosolic compartments in the fluorescent image. The scale bar represents 20 μm.

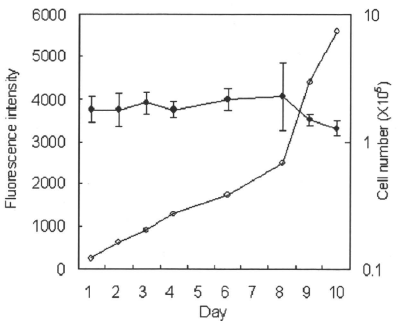

Figure 3. Changes in fluorescence intensity of **4d** existing in total NIH-3T3 cells in culture (solid circle) and the number of cells (open circle) measured over the course of the 10 days following electroporation. Fluorescence intensity is proportional to the amount of **4d** in total cells.

cells. The number of cells transplanted to the rat ischemic hind limb model (27) or infarcted myocardium swine model (28) was 1×10^7 or 5×10^7, respectively. The sensitivity shown in Fig. 4 revealed that our imaging agent would surely be useful for tracking this range of transplanted cells *in vivo*. Future studies should focus on high labeling efficiency at higher concentrations of **4d** using electroporation or another method.

2.5. *In vivo* fate of free SPIO and free Gd–PVA

To detect the living cells, contrast agents present outside of the labeled cells (free contrast agent) after cell death should be eliminated from the transplantation site. Solutions of **4d** and SPIO injected into the tissue were used as the model for free contrast agents. Solutions of **4d** and SPIO were directly injected into rat femoral muscles, and on days 0, 3 and 6, the MR image was analyzed (Fig. 5). Representative slices are shown in Fig. 5. The bright signal attributed to **4d** weakened rapidly and was observed only slightly on day 3. In contrast, the dark signal due to SPIO remained in the same area and was clearly observed even 10 days after the injection. The same tendency was observed in the other slices. SPIO-derived contrast several days after injection may be attributed to the phagocytes engulfing the injected SPIO, as has been previously reported (22,23). Furthermore, the time courses of the contrast-to-noise ratio (CNR) and the volume of the contrast-enhanced region were evaluated (Fig. 6). For SPIO, the CNR and the volume of the contrast-enhanced region showed no significant decrease over the course of 13 days. In contrast, these same parameters decreased rapidly when **4d** was used. Signal enhancement was observed in only one out of three rats at 4 days after injection. Therefore, the data of **4d** at 4 days have no error bar. Signal

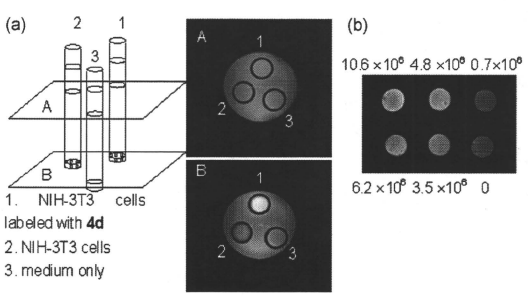

Figure 4. (a) *In vitro* T_1-weighted MR measurements of **4d**-labeled NIH-3T3 cells (tube 1), unlabeled NIH-3T3 (tube 2), and medium (tube 3) at 4.7 T. (b) *In vitro* T_1-weighted image of different numbers of cells labeled with **4d** suspended in 100 μl agarose gel.

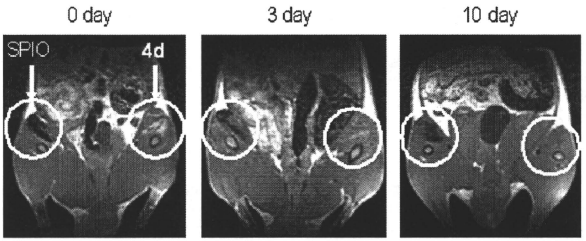

Figure 5. *In vivo* MR measurements after the injection of **4d** solution and SPIO solution into rat femoral muscle at 1.5 T. These images showed the slices passing though the injection site. These images were obtained with a TR of 1500 ms and a TE of 9 ms (FOV, 4 × 8 cm; matrix, 128 × 256; slice thickness, 1 mm; slice gap, 0 mm; number of slices, 35).

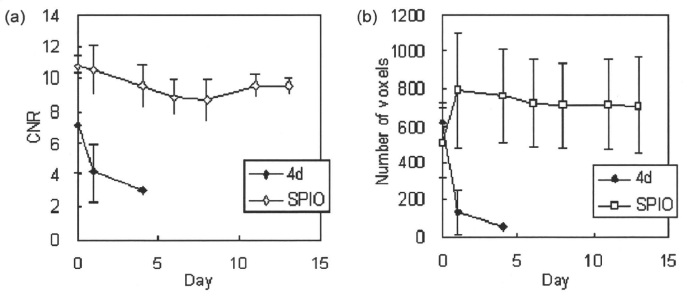

Figure 6. The time course of (a) the contrast-to-noise ratio (CNR) and (b) the number of voxels in the region where bright or dark signals due to contrast agents were observed. Contrast enhancement due to **4d** and SPIO was assessed using T_1- (TE 9 ms, TR 500 ms) and T_2- (TE 20 ms, TR 3 s) weighted images, respectively. The other scanning parameters were the same as in Figure 5. Three rats were examined and treated in the same manner as in Figure 5. CNR was calculated as $(\pi/2)^{1/2}|S_1\text{-}S_2|/S_{air}$, where S_1, S_2 and S_{air} were the mean intensities in the contrast-enhanced region, muscle and air, respectively.

enhancement due to **4d** disappeared completely in all rats at 6 days after injection. These data showed the rapid clearance of Gd–PVA from muscle and the long-term retention of SPIO in muscle. Yamaoka *et al.* reported that the half-life period of radio-labeled PVA (molecular weight of 74 800) after i.m. injection was about 10 h (38). As shown in Fig. 6, the half-life period of free Gd–PVA from the tissue was about 10 hs, which was almost the same as that of PVA. This result suggested that free Gd–PVA behaved like free PVA without interacting with macrophages *in vivo*. It can then be considered that the MR contrast of Gd–PVA is attributable to the living cells *in vivo*.

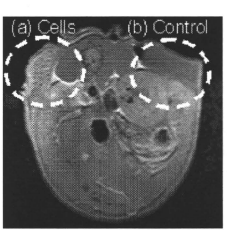

Figure 7. Preliminary *in vivo* T_1-weighted MR measurements of **4d**-labeled NIH-3T3 cells implanted in mice subcutaneously at 2 T. These cells were fixed in agarose gel. (a) 2×10^7 of **4d**-labeled cells suspended in 200 μl agarose gel (b) 200 μl agarose gel only. T_1-weighted images were acquired using a 2D spin echo sequence with a TR of 2000 ms and a TE of 9 ms (FOV, 3 × 6 cm; matrix, 128 × 256; slice thickness, 1 mm) at room temperature.

2.6. Preliminary *in vivo* MR imaging of transplanted NIH-3T3 cells

Figure 7 shows an MR image of a rat that received subcutaneous transplantation of 2×10^7 **4d**-labeled NIH-3T3 cells entrapped in agarose gel and cell-free gel (control) at each side of the back. In this preliminary MR imaging, we used undegradable agarose gel to evaluate the MRI contrast at a known density of cells. Strong contrast enhancement was observed at the area where labeled NIH-3T3 cells were transplanted, while the control gel revealed a dark shadow. These results indicate that transplanted cells can be detected *in vivo* at a cell density of 10^7 cells per 0.1 ml.

3. DISCUSSION

Our goal was to track only the living cells *in vivo* for a long period of time. To this end, an MRI contrast agent with adequate

characteristics for cell labeling and delivery system into the cells is a key factor. Cell labeling using SPIO as a contrast agent was reported in detail by Engberink *et al.* in 2007 (29). They cocultured human monocytes with SPIO suspension at a concentration of 1.0 mg Fe ml^{-1} for 0–6 h. Incubation with SPIO resulted in effective cell labeling by endocytosis, nonspecifically. The detection limit was 0.5×10^6 labeled cells per 250 μl on a 4.7 T MRI scanner. SPIO permits the detection of a small number of cells because of its high sensitivity. In general, however, endocytosed substrates would be exocytosed over time. The MR contrast obtained after SPIO-labeled cell transplantation was not attributed to the transplanted cells but to the macrophages that engulfed the free SPIO (22,23). In this study, MR imaging data for SPIO solution in femoral muscle showed that, even at 10 days after injection, SPIO still remained. These data suggested that SPIO is less suitable for long-term cell tracking. To track the transplanted cells for a long period of time, the labeling agent released upon cell death should be eliminated from the tissue.

Since we found that low-molecular-weight Gd-chelates cannot remain in cells stably (data not shown), water-soluble conjugates of Gd-chelates and a bio inert water-soluble carrier were designed. The characteristics of Gd-containing conjugates including the body distribution pattern are affected by the nature of the carrier polymer. The water-soluble contrast agent is expected to be eliminated from the body once it exits the cells if a truly bio-inert carrier molecule is selected. To track only the living cells, the contrast agents should be designed to be different from the conventional water-soluble imaging agent for vascular inflammation imaging or vascular imaging (30–36).

We selected PVA in this experiment as the carrier material for long-term living cell tracking. Selecting nondegradable PVA as the carrier enabled us to evaluate the potential of the contrast agent in intracellular distribution or in cell tracking for a long period of time. The body distribution of various polymeric carriers has been extensively studied (37,38). Among these carriers, PVA has various advantages as a candidate for use in the biomedical and pharmaceutical fields. Some of these advantages include its characteristics of water solubility, nontoxicity and noncarcinogenicity. The half-life of Gd–PVA was longer than those of other polymers such as dextran, pullulan and gelatin because of an insignificant interaction with macrophages and blood cells (24). This weak interaction with various cells is believed to be responsible for the high hydrophilicity of PVA. Since we proposed novel contrast agents in the present study that would not exit the cells for long-term cell tracking, this weak interaction with the cell membrane was considered to be an advantage.

In the present study, we chose electroporation as a method for delivering Gd–PVA into cells in order to establish a method that is applicable to a variety of cells such as stem cells and primary cells. The material delivery efficiency into cells via nonspecific endocytosis or receptor-mediated encodytosis is probably affected by the cell type. Interestingly, Gd–PVA delivered into cells was localized only in the cytosolic compartment even after cell proliferation (Fig. 2), although the reason for this remains unclear.

One possible issue in living cell tracking, although unlikely to occur, is the uptake of dying cells labeled with **4d** by tissue macrophages that remain in the tissue. To study this possibility, it is necessary to perform an experiment using cells in different states (viable, dying and dead). However, it is difficult to control the states of transplanted cells. We are considering evaluating the effect of macrophages on the fate of Gd–PVA by transplanting irradiated cells with sublethal doses or by xenografting Gd–PVA-labeled cells.

Long-term cell tracking will be feasible due to the high stability of Gd–PVA in cells for a long period of time (Fig. 3). In contrast to SPIO, the free Gd–PVA will be eliminated from the tissue (Fig. 5) when the transplanted cells burst upon cell death. The imaging of only the living cells might be achieved using Gd–PVA.

4. CONCLUSION

The novel MRI contrast agents composed of PVA and Gd showed high relaxivity and low cytotoxicity. The growing rate of NIH-3T3 cells was not affected by the intracellularly delivered Gd–PVA. Furthermore, Gd–PVA was retained stably in cells for at least 10 days. The *in vitro* T_1-weighted MR measurements using NIH-3T3 cells revealed that cells could be visualized under MRI. This *in vivo* study demonstrates for the first time that Gd–PVA has high applicability as a novel contrast agent for tracking only living cells.

5. MATERIALS AND METHODS

5.1. Materials

PVA (M_w: 74,800, degree of saponification 98%) was a kind gift from Kuraray Co. Ltd (Okayama, Japan). 1,4,7,10-Tetraazacyclododecane-1,4,7,10-tetraacetic acid mono(*N*-hydroxysuccinimidyl ester) (DOTA-NHS-ester) was purchased from Macrocyclics (Dallas, TX, USA). FITC-NHS-ester was purchased from Invitrogen (Eugene, OR, USA). Gadolinium chloride ($GdCl_3$) was purchased from Wako Pure Chemical Industries (Osaka, Japan). Resovist was purchased from Nihon Schering (Osaka, Japan). Other reagents and solvents were commercially available and used as received.

5.2. Synthesis of Gd–PVA

The synthetic route and structure of polymeric contrast agents with different introduction ratios of Gd are shown in Scheme 1. A mixture of PVA (**1**; 0.44 g, 10 mmol in monomer unit concentration) and carbonyl diimidazole (5, 7.5, and 10 mmol) was stirred in 80 ml of anhydrous dimethylsulfoxide (DMSO) at room temperature under a nitrogen atmosphere for 4 h. Then, 1,3-propanediamine (50, 75, and 100 mmol) was added to the mixture, further stirred at room temperature for 1 day, and dialyzed with Spectra/Pore membrane (cut-off molecular weight $= 1 \times 10^4$; Spectrum Laboratories Inc., Rancho Dominguez, CA, USA) in distilled water three times. The remaining solution was lyophilized to give **2**.

^{1}H NMR (D_2O): $\delta = 4.92$ (br, CH_2CHO), 3.92 (br, CH_2CHOH), 3.10 [br, $C(=O)NHCH_2$], 2.79 (br, CH_2NH_2), 1.57 (br, $CHCH_2$, br, $CH_2CH_2CH_2$). The introduction ratios were calculated as the ratio of the integrals of the peaks at 2.79 and 1.57 ppm.

PVA-diamine was reacted with DOTA-NHS-ester (NH_2 of FITC-PVA-diamine: DOTA-NHS-ester = 1:1.5) in 80 ml of anhydrous DMSO at room temperature for 1 day under a nitrogen atmosphere. The reaction mixture was dialyzed in distilled water three times, and lyophilized to give PVA-diamine-DOTA (**3**).

^{1}H NMR (D_2O): $\delta = 5.07$ (br, CH_2CHO), 4.06 (br, CH_2CHOH), 3.86 [br, $C(=O)CH_2N$)] 3.51 [br, $NCH_2C(=O)OH$], 3.24 [br, $C(=O)NHCH_2$, br, CH_2CH_2N], 1.69 (br, $CHCH_2$, br, $CH_2CH_2CH_2$).

The solution of **3** was then treated with the dropwise addition of 1.5 mole equiv. of gadolinium chloride to the DOTA while stirring. The pH was maintained between 6.6 and 7.0 with 1 M NaOH solution and stirred for an additional 24 h at room temperature. The reaction mixture was dialyzed in distilled water three times and lyophilized to give Gd–PVA (**4a–d**).

For labeling Gd–PVA with FITC, PVA–diamine was mixed with a small amount of FITC–NHS–ester (NH_2 of **2**: FITC–NHS–ester = 1: 8×10^{-5}) and stirred in 80 ml of anhydrous DMSO at room temperature for 1 day under a nitrogen atmosphere. The reaction mixture was dialyzed, lyophilized to give FITC-PVA-diamine and subjected to the DOTA reaction as shown in Scheme 1.

5.3. Measurements

^{1}H-NMR spectra were recorded on a 300 MHz NMR spectrometer (Gemini2000/300; Varian Inc., CA, USA) with a sample concentration of 8 mg per 800 μl. Size exclusion chromatography analysis was carried out using Shimadzu Gel Permeation Chromatography System apparatus equipped with a refractive index and UV detectors under the following conditions: TSKgel G6000PWXL and G3000PWXL columns and 0.067 M PBS eluent at a flow rate of 0.3 ml min^{-1} at 40°C (Tosoh, Tokyo, Japan) with a sample concentration of 1 mg per 100 μl. The concentration of the paramagnetic species [Gd(III)] was measured by inductively coupled plasma atomic emission spectroscopy (model 7510, Shimadzu Co., Kyoto, Japan).

5.4. Relaxivity of conjugated Gd at 7.1 T

Solvent longitudinal relaxation times (T_1) in the aqueous solutions of the gadolinium conjugate were measured at different concentrations of gadolinium conjugate using a mixture of distilled water (0.625%) and deuterium oxide (99.375%) as a solvent. All measurements were performed on a 300 MHz (7.1 T) NMR spectrometer (Gemini2000/300; Varian Inc., CA, USA) using an inversion recovery technique with 19 inversion times (*TI*) ranging from 1 to 5000 ms at ambient temperature (25°C) with a sample concentration of 8 mg per 800 μl. A typical pulse width of 180° pulse was 19 μs. T_1 values were estimated using least-squares fitting of the signal intensities measured at 19 *TI* values in an exponential fashion. The relaxivity of each gadolinium complex was determined by a linear regression of the $1/T_1$ vs the gadolinium complex concentration.

5.5. Cell culture

NIH-3T3 cells were used for evaluating the cytotoxicity, cell labeling potential and imaging efficiency of the Gd–PVA. They were grown in Dulbecco's modified Eagle's medium (DMEM-LG) supplemented with 10% bovine calf serum, 100 units ml^{-1} penicillin, and 100 units ml^{-1} streptomycin at 37°C, 10% CO_2 atmosphere.

5.6. Cytotoxicity assay

NIH-3T3 cells (1×10^4 cells per well) were seeded in a 96-well culture plate and cultured overnight. Varying concentrations (polymer unit concentrations of 10 nM to 10 mM) of **4b** were added to each well. At the indicated time points, the number of cells was measured by WST-1 assay according to the manufacturer's protocol (Takara Shuzo, Otsu, Japan). Briefly, cells were washed with PBS three times, and the culture medium (100 μl) was added to each well. Ten microliters of WST-1 {4-[3-(4-iodophenyl)-2-(4-nitrophenyl)-2H-5-tetrazolio]-1,3-benzene disulfonate} solution was added to each well, and the plates were incubated for 30 min. The absorbance at 450 nm was measured on a microplate reader (Model 550, Bio-Rad Laboratory Co., Tokyo, Japan).

5.7. Cell labeling by electroporation

NIH-3T3 cells were cultured in a 6 cm diameter Petri dish at a concentration of 5×10^5 cells per dish in DMEM-LG for 1 day. An arbitrary amount of **4d** was added to the culture medium, and electrical pulses were applied to cells using a CUY-21 electroporator (CUY-21; NEPPA GENE, Tokyo, Japan). Rectangular electrical pulses (field strength 300 V cm^{-1}, number of pulses 10, pulse duration 5 ms) were applied to cells using two parallel electrodes with a 5 mm gap. Cells were incubated for 1 h and washed with PBS twice.

5.8. Stability of 4d in cells

To determine whether **4d** molecules stay in NIH-3T3 cells for a long period of time, the labeled cells (1×10^4 cells) were seeded in a 6 cm diameter Petri dish and cultured over 10 days without a subculture. The time course of the fluorescence intensity for the cultured cells was measured as follows. Before each measurement, cells in one dish were washed three times with PBS to eliminate the free **4d** from the cells and lysed in 1 ml lysis buffer [25 mM tris (pH 7.8), 2 mM dithiothreitol, 2 mM 1,2-diaminocyclohexan-*N*,*N*,*N*′,*N*′-tetraacetic acid, 10% glycerol, 1% Triton X-100]. After 1 h incubation at 37°C, the fluorescence intensity of the cell lysates was measured with a spectrofluorometer (excitation 430 nm, emission 540 nm, Wallac 1420 ARVOsx, Perkin-Elmer Life Sciences, Boston, MA, USA). The time course of the fluorescence intensity represented the stability of **4d** in the cells. At the same time, the number of cells in each dish was counted. In addition, the amount of **4d** delivered into each cell by electroporation was calculated using the standard curve of fluorescence intensity.

5.9. MR imaging of Gd–PVA solution at 4.7 T

MR images of **4d** aqueous solutions were obtained on a 200-MHz (4.7 T) NMR spectrometer (Apollo; Tecmag Inc., TX, USA) equipped with a gradient system (Jeol Ltd, Tokyo, Japan; maximum gradient strength 20 mT m^{-1}; slew late 50 mT m^{-1} ms^{-1}) using a saddle coil with an inner diameter of 47 mm. Aqueous solutions with different concentrations (0.05, 0.1, 0.2, 0.3, 0.5 and 1 mM) of polymer unit were prepared. Three test tubes with different concentrations were fixed vertically. A horizontal section was scanned. T_1-weighted images of the samples were acquired using a 2D spin echo sequence with a repetition time (*TR*) of 2000 ms and an echo time (*TE*) of 16 ms. Taking the long T_1 of the water observed in the 1.5 T machine into account, *TR* was greater in comparison to that for general T_1-weighted images. We used the minimum possible *TE* to minimize the T_2 relaxation effect. Other scanning parameters were as follows: field of view (FOV), 6 × 6 cm; matrix, 256 × 256; slice thickness, 1 cm.

5.10. MR imaging of NIH-3T3 cells *in vitro*

MR measurements of labeled cells were performed using the same scanner and the same parameters as in the imaging of **4d** solutions. Cells labeled with **4d** by electroporation were trypsinized, centrifuged and resuspended in test tubes (75 mm

long, 10 mm in diameter) at 7×10^6 cells in 2 ml of complete DMEM. The test tubes with labeled cell suspensions were allowed to settle for 1 day to allow the cells to be precipitated before MR imaging. A test tube with unlabeled cell suspensions was also prepared in the same manner. In addition, a test tube with cell-free pure medium was prepared. The three test tubes prepared were arranged as shown in Fig. 4(a). Scanned slices were positioned so that they pass through the cell pellet part (slice B in Fig. 4a) or the solution part (slice A in Fig. 4a).

The cell density dependence of signal enhancement was examined as follows. Different numbers of labeled cells were suspended in 100 μl of agarose solution at the concentration of 2 wt% and cooled to be gelated. The MR imaging data of these mixtures were collected by a 1 T compact MR imaging system with a permanent magnet (MRmini, Dainippon Sumitomo Pharma, Osaka, Japan) with a *TE* of 9 ms and a *TR* of 1500 ms (FOV, 3 × 6 cm; matrix, 128 × 256; slice thickness, 3.7 mm).

5.11. *In vivo* fate of free SPIO and free Gd–PVA

The clearance of **4d** and SPIO after intramuscular injection was investigated in male rat F344. The rat was anesthetized by inhalation anesthesia (1.5% isoflurane). Solutions of **4d** (Gd 0.8 μmol per 50 μl water) and carboxydextran-coated SPIO, Resovist™ (Fe 0.8 μmol per 50 μl water, Bayer, Osaka, Japan) were injected into the left and right femoral muscles, respectively, using a 29 G needle. Whole inferior limbs of the animal were scanned at 0, 3 and 10 days after injection on a 1.5 T compact MR imaging system. These images were obtained with a *TR* of 1500 ms and a *TE* of 9 ms (FOV, 4 × 8 cm; matrix, 128 × 256; slice thickness, 1 mm; slice gap, 0 mm; number of slice, 35).

For the time course of the CNR and the number of voxels in the region, whole inferior limbs of the animal were scanned at 0, 1, 4, 6, 8, 11 and 13 days after injection on a 1.5 T compact MR imaging system. These images were obtained with a *TR* of 500 ms and a *TE* of 9 ms, and with a *TR* of 3000 ms and a *TE* of 20 ms (FOV, 4 × 8 cm; matrix, 128 × 256; slice thickness, 1 mm; slice gap, 0 mm; number of slices, 35). CNR was calculated as $(\pi/2)^{1/2}|S_1-S_2|/S_{air}$, where S_1, S_2 and S_{air} were the mean intensities in the contrast-enhanced region, muscle and air, respectively.

5.12. Preliminary MR imaging of transplanted NIH-3T3 cells

In vivo cell tracking was preliminarily performed in male Balb/c mice. These mice were anesthetized for imaging with the use of a general inhalation anesthesia (1.5% isoflurane) and were allowed to breathe spontaneously during preparation and scanning. NIH-3T3 cells labeled with **4d** (2×10^7 cells) were embedded in 2 wt% agarose gel (200 μl) and transplanted to the mice subcutaneously. MR images were obtained using a 2 T compact MR imaging system with a permanent magnet. T_1-weighted images were acquired using a 2D spin echo sequence with a *TR* of 2000 ms and a *TE* of 9 ms (FOV, 3 × 6 cm; matrix, 128 × 256; slice thickness, 1 mm) at room temperature.

6. SUPPORTING INFORMATION

Supporting information can be found in the online version of this article.

Acknowledgements

This work was supported by grants-in-aid from the Ministry of Health, Labour and Welfare of Japan (Health and Labour Sciences Research Grants, Research on Nanotechnical Medical). This work was also supported by a Research Grant for Cardiovascular Diseases (18A-2) from the Ministry of Health, Labour and Welfare of Japan.

References

1. Perin EC, Dohmann HF, Borojevic R, Silva SA, Sousa AL, Mesquita CT, Rossi MI, Carvalho AC, Dutra HS, Dohmann HJ, Silva GV, Belem L, Vivacqua R, Rangel FO, Esporcatte R, Geng YJ, Vaughn WK, Assad JA, Mesquita ET, Willerson JT., Transendocardial, autologous bone marrow cell transplantation for severe, chronic ischemic heart failure. Circulation 2003; 107 18 2294–2302.
2. Schmid C, Schleuning M, Schwerdtfeger R, Hertenstein B, Mischak-Weissinger E, Bunjes D, Harsdorf SV, Scheid C, Holtick U, Greinix H, Keil F, Schneider B, Sandherr M, Bug G, Tischer J, Ledderose G, Hallek M, Hiddemann W, Kolb HJ. Long-term survival in refractory acute myeloid leukemia after sequential treatment with chemotherapy and reduced-intensity conditioning for allogeneic stem cell transplantation. Blood 2006; 108(3): 1092–1099.
3. Slavin S, Nagler A, Naparstek E, Kapelushnik Y, Aker M, Cividalli G, Varadi G, Kirschbaum M, Ackerstein A, Samuel S, Amar A, Brautbar C, Ben-Tal O, Eldor A, Or R. Nonmyeloablative stem cell transplantation and cell therapy as an alternative to conventional bone marrow transplantation with lethal cytoreduction for the treatment of malignant and nonmalignant hematologic diseases. Blood 1998; 91(3): 756–763.
4. Kim SW, Han H, Chae GT, Lee SH, Bo S, Yoon JH, Lee YS, Lee KS, Park HK, Kang KS. Successful stem cell therapy using umbilical cord blood-derived multipotent stem cells for Buerger's disease and ischemic limb disease animal model. Stem Cells 2006; 24(6): 1620–1626.
5. Stamm C, Westphal B, Kleine HD, Petzsch M, Kittner C, Klinge H, Schumichen C, Nienaber CA, Freund M, Steinhoff G. Autologous bone-marrow stem-cell transplantation for myocardial regeneration. Lancet 2003; 361(9351): 45–46.
6. Strauer BE, Brehm M, Zeus T, Kostering M, Hernandez A, Sorg RV, Kogler G, Wernet P. Repair of infarcted myocardium by autologous intracoronary mononuclear bone marrow cell transplantation in humans. Circulation 2002; 106(15): 1913–1918.
7. Grant MB, May WS, Caballero S, Brown GA, Guthrie SM, Mames RN, Byrne BJ, Vaught T, Spoerri PE, Peck AB, Scott EW. Adult hematopoietic stem cells provide functional hemangioblast activity during retinal neovascularization. Nat Med 2002; 8(6): 607–612.
8. Tang YL, Zhao Q, Qin X, Shen L, Cheng L, Ge J, Phillips MI. Paracrine action enhances the effects of autologous mesenchymal stem cell transplantation on vascular regeneration in rat model of myocardial infarction. Ann Thorac Surg 2005; 80(1): 229–236 discussion 236-227.
9. Beeres SL, Bengel FM, Bartunek J, Atsma DE, Hill JM, Vanderheyden M, Penicka M, Schalij MJ, Wijns W, Bax JJ. Role of imaging in cardiac stem cell therapy. J Am Coll Cardiol 2007; 49(11): 1137–1148.
10. Frangioni JV, Hajjar RJ. In vivo tracking of stem cells for clinical trials in cardiovascular disease. Circulation 2004; 110(21): 3378–3383.
11. Tanaka M, Swijnenburg RJ, Gunawan F, Cao YA, Yang Y, Caffarelli AD, de Bruin JL, Contag CH, Robbins RC. In vivo visualization of cardiac allograft rejection and trafficking passenger leukocytes using bioluminescence imaging. Circulation 2005; 112(9 Suppl): I105–110.
12. Wang X, Rosol M, Ge S, Peterson D, McNamara G, Pollack H, Kohn DB, Nelson MD, Crooks GM. Dynamic tracking of human hematopoietic stem cell engraftment using in vivo bioluminescence imaging. Blood 2003; 102(10): 3478–3482.

13. Sutton EJ, Henning TD, Pichler BJ, Bremer C, Daldrup-Link HE. Cell tracking with optical imaging. Eur Radiol 2008; 18(10): 2021–2032.
14. Takagi Y, Takahashi J, Saiki H, Morizane A, Hayashi T, Kishi Y, Fukuda H, Okamoto Y, Koyanagi M, Ideguchi M, Hayashi H, Imazato T, Kawasaki H, Suemori H, Omachi S, Iida H, Itoh N, Nakatsuji N, Sasai Y, Hashimoto N. Dopaminergic neurons generated from monkey embryonic stem cells function in a Parkinson primate model. J Clin Invest 2005; 115(1): 102–109.
15. Takahashi M, Nakamura T, Toba T, Kajiwara N, Kato H, Shimizu Y. Transplantation of endothelial progenitor cells into the lung to alleviate pulmonary hypertension in dogs. Tissue Eng 2004; 10(5–6): 771–779.
16. Tomita S, Mickle DA, Weisel RD, Jia ZQ, Tumiati LC, Allidina Y, Liu P, Li RK. Improved heart function with myogenesis and angiogenesis after autologous porcine bone marrow stromal cell transplantation. J Thorac Cardiovasc Surg 2002; 123(6): 1132–1140.
17. Kraitchman DL, Tatsumi M, Gilson WD, Ishimori T, Kedziorek D, Walczak P, Segars WP, Chen HH, Fritzges D, Izbudak I, Young RG, Marcelino M, Pittenger MF, Solaiyappan M, Boston RC, Tsui BM, Wahl RL, Bulte JW. Dynamic imaging of allogeneic mesenchymal stem cells trafficking to myocardial infarction. Circulation 2005; 112(10): 1451–1461.
18. Hill JM, Dick AJ, Raman VK, Thompson RB, Yu ZX, Hinds KA, Pessanha BS, Guttman MA, Varney TR, Martin BJ, Dunbar CE, McVeigh ER, Lederman RJ. Serial cardiac magnetic resonance imaging of injected mesenchymal stem cells. Circulation 2003; 108(8): 1009–1014.
19. Rice HE, Hsu EW, Sheng H, Evenson DA, Freemerman AJ, Safford KM, Provenzale JM, Warner DS, Johnson GA. Superparamagnetic iron oxide labeling and transplantation of adipose-derived stem cells in middle cerebral artery occlusion-injured mice. AJR Am J Roentgenol 2007; 188(4): 1101–1108.
20. Stuckey DJ, Carr CA, Martin-Rendon E, Tyler DJ, Willmott C, Cassidy PJ, Hale SJ, Schneider JE, Tatton L, Harding SE, Radda GK, Watt S, Clarke K. Iron particles for noninvasive monitoring of bone marrow stromal cell engraftment into, and isolation of viable engrafted donor cells from, the heart. Stem Cells 2006; 24(8): 1968–1975.
21. Hoshino K, Ly HQ, Frangioni JV, Hajjar RJ. In vivo tracking in cardiac stem cell-based therapy. Prog Cardiovasc Dis 2007; 49(6): 414–420.
22. Amsalem Y, Mardor Y, Feinberg MS, Landa N, Miller L, Daniels D, Ocherashvilli A, Holbova R, Yosef O, Barbash IM, Leor J. Iron-oxide labeling and outcome of transplanted mesenchymal stem cells in the infarcted myocardium. Circulation 2007; 116(11 Suppl): I38–45.
23. Li Z, Suzuki Y, Huang M, Cao F, Xie X, Connolly AJ, Yang PC, Wu JC. Comparison of reporter gene and iron particle labeling for tracking fate of human embryonic stem cells and differentiated endothelial cells in living subjects. Stem Cells 2008; 26(4): 864–873.
24. Yamaoka T, Tabata Y, Ikada Y. Comparison of body distribution of poly(vinyl alcohol) with other water-soluble polymers after intravenous administration. J Pharm Pharmacol 1995; 47(6): 479–486.
25. Walczak P, Kedziorek DA, Gilad AA, Lin S, Bulte JW. Instant MR labeling of stem cells using magnetoelectroporation. Magn Reson Med 2005; 54(4): 769–774.
26. Pillai O, Panchagnula R. Polymers in drug delivery. Curr Opin Chem Biol 2001; 5(4): 447–451.
27. Li TS, Hamano K, Suzuki K, Ito H, Zempo N, Matsuzaki M. Improved angiogenic potency by implantation of ex vivo hypoxia prestimulated bone marrow cells in rats. Am J Physiol Heart Circ Physiol 2002; 283(2): H468–473.
28. Zhang S, Ge J, Zhao L, Qian J, Huang Z, Shen L, Sun A, Wang K, Zou Y. Host vascular niche contributes to myocardial repair induced by intracoronary transplantation of bone marrow CD34+ progenitor cells in infarcted swine heart. Stem Cells 2007; 25(5): 1195–1203.
29. Oude Engberink RD, van der Pol SM, Dopp EA, de Vries HE, Blezer EL., Comparison of SPIO and USPIO for in vitro labeling of human monocytes: MR detection and cell function. Radiology 2007; 243(2): 467–474.
30. Aime S, Cabella C, Colombatto S, Geninatti Crich S, Gianolio E, Maggioni F. Insights into the use of paramagnetic Gd(III) complexes in MR-molecular imaging investigations. J Magn Reson Imag 2002; 16(4): 394–406.
31. Gustafsson B, Youens S, Louie AY. Development of contrast agents targeted to macrophage scavenger receptors for MRI of vascular inflammation. Bioconjug Chem 2006; 17(2): 538–547.
32. Langereis S, de Lussanet QG, van Genderen MH, Meijer EW, Beets-Tan RG, Griffioen AW, van Engelshoven JM, Backes WH. Evaluation of Gd(III)DTPA-terminated poly(propylene imine) dendrimers as contrast agents for MR imaging. NMR Biomed 2006; 19(1): 133–141.
33. Lu ZR, Wang X, Parker DL, Goodrich KC, Buswell HR. Poly(-l-glutamic acid) Gd(III)-DOTA conjugate with a degradable spacer for magnetic resonance imaging. Bioconjug Chem 2003; 14(4): 715–719.
34. Nakamura E, Makino K, Okano T, Yamamoto T, Yokoyama M. A polymeric micelle MRI contrast agent with changeable relaxivity. J Control Release 2006; 114(3): 325–333.
35. Wen X, Jackson EF, Price RE, Kim EE, Wu Q, Wallace S, Charnsangavej C, Gelovani JG, Li C. Synthesis and characterization of poly(L-glutamic acid) gadolinium chelate: a new biodegradable MRI contrast agent. Bioconjug Chem 2004; 15(6): 1408–1415.
36. Yan GP, Liu ML, Li LY. Polyaspartamide gadolinium complexes containing sulfadiazine groups as potential macromolecular MRI contrast agents. Bioconjug Chem 2005; 16(4): 967–971.
37. Yamaoka T, Tabata Y, Ikada Y. Distribution and tissue uptake of poly(ethylene glycol) with different molecular weights after intravenous administration to mice. J Pharm Sci 1994; 83(4): 601–606.
38. Yamaoka T, Tabata Y, Ikada Y. Fate of water-soluble polymers administered via different routes. J Pharm Sci 1995; 84(3): 349–354.

＊ 研究論文 ＊

頭部SPECTにおけるコリメータ開口補正およびモンテカルロ法に基づく散乱線補正を用いた画像再構成法の定量精度評価

崎本 智則[*1] 銭谷 勉[*2] 石田 健二[*3] 渡部 浩司[*2]
平野 祥之[*2] Antti SOHLBERG[*2] 湊 小太郎[*1] 飯田 秀博[*2]

要 旨

近年，我々はコリメータ開口補正による解像度補正，吸収補正，モンテカルロ法に基づいた散乱線補正機構を搭載した画像再構成法を開発し，シミュレーション評価によりその有効性を明らかにしてきた．だが，実際の実験による検証は今まで行われてこなかった．本研究では，一連のファントム実験を行い，本画像再構成法の定量精度を検証した．東芝製SPECT装置GCA7200Aを用いて，線線源ファントムによる空間解像度の検証，濃度一様プールファントムによる一様性の検証，脳ファントムによる画像コントラストおよび放射能濃度に対する比例性の評価を行った．実験の結果，本再構成法によって，補正無しで8.8 mm程度だった解像度は3.5 mm程度に改善し，濃度一様ファントムの画素値の変動は13%から10%以下に改善した．放射能濃度の比例性の誤差も35%から12%まで改善され，それに伴い，画像コントラストも大きく改善した．本検証実験によって，本手法の吸収補正と散乱線補正の妥当性が確認でき，解像度補正の効果が大きな利点と考えられた．この結果より，本手法が局所脳機能画像定量SPECTに貢献することが期待される．

キーワード：SPECT，定量性，散乱線補正，モンテカルロ法，コリメータ開口補正
Med Imag Tech **28**(2)：135-144, 2010

1. はじめに

SPECT(single photon emission computed tomography)では，コリメータの開口によって空間解像度が低下する．また，被写体内でのガンマ線の吸収および散乱によって，定量性が低下する．

これまでに，コリメータ開口補正（collimator-detector response compensation; CDRC），吸収補正(attenuation compensation; AC)，散乱線補正(scatter compensation; SC)を含むSPECT画像再構成法が開発されてきたが，ほとんどが心臓SPECTを対象に評価されてきた〔1~4〕．

我々も，吸収補正，コリメータ開口補正〔5〕，モンテカルロ法に基づく散乱線補正（Monte Carlo-based scatter compensation; MCSC）を組み込んだ画像再構成法を開発し，シミュレーションによりその有効性を明らかにしてきた〔6〕．本研究では，我々が開発した画像再構成法の頭部SPECTにおける実用化を目指し，一連の物理ファントム実験を行い，定量精度を検証した．

[*1] 奈良先端科学技術大学院大学情報科学研究科〔〒630-0192 奈良県生駒市高山町8916-5〕
[*2] 国立循環器病センター研究所先進医工学センター放射線医学部
e-mail: tomonori-s@is.naist.jp
[*3] ㈱モレキュラーイメージングラボ
投稿受付：2009年5月15日
最終稿受付：2009年12月11日
採用決定日：2010年1月18日

2. 方 法

1）画像再構成法

本手法では，OS-EM(ordered subset expectation maximization)〔7〕法を画像再構成に用い，順投影部分に散乱線分布を加えることにより散乱線補正を行った．順投影部分に散乱線分布を加えたOS-EM法の漸化式は，式(1)のように表わされる．

$$\lambda_j^{n+1} = \frac{\lambda_j^n}{\sum_{i \in S_n} a_{ij}} \sum_{i \in S_n} \frac{a_{ij} y_i}{\sum_k a_{ik} \lambda_k^n + s_i} \qquad (1)$$

ここでjおよびkは再構成画素の通し番号，iは検出器画素の通し番号，a_{ij}は画素jから放出されたガンマ線が検出器iで検出される確率，yは

計測により得た投影データ，λは再構成画像，sは散乱線投影分布，S_nはn番目のサブセットである．OS-EM法では，一回の反復で，サブセットの数と同じ回数だけ画像が更新される．吸収補正およびコリメータ開口補正は，以下に述べるように，検出確率a_{ij}に吸収およびコリメータ応答のモデルを組み込むことにより実装された．また本手法では，吸収，散乱，コリメータ開口の各補正を簡単に実装するために，画像マトリクスを回転してから順投影および逆投影を行うRotation-based法〔8〕を用いた．

2）コリメータ開口補正

SPECTガンマカメラの分解能は検出器の固有分解能およびコリメータ特性により決定される．一般にパラレルホールコリメータにおけるコリメータ応答関数（collimator-detector response function; CDRF）は二次元のガウシアン関数とみなすことができる．また，コリメータ応答関数の半値幅（full width at half maximum; FWHM）は，検出器と線源との間の距離に比例して直線的に大きくなると仮定できるので，

$$FWHM(d) = \alpha d + \beta \tag{2}$$

で表わすことができる〔9〕．ここでdは検出器と線源の間の距離である．αとβの値を実験的に求めることにより，コリメータ応答関数は線源と検出器の距離に依存した線形モデルとして表すことができる．

Fig. 1で示すように変数を定義したとき，コリメータ応答関数は，

$$h(x,y,d) = \frac{1}{2\pi\sigma^2(d)}\exp\left(-\frac{r^2}{2\sigma^2(d)}\right) \tag{3}$$

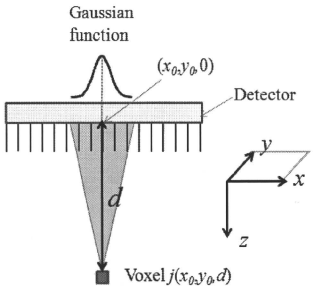

Fig. 1 Collimator-detector response function (CDRF).

と表される．ここでσはガウシアン関数の標準偏差で，ガウシアン関数の半値幅の約0.425倍となる．rは線源から最短距離にある検出器面上の点$(x_0,y_0,0)$と，検出器面上のある点$(x,y,0)$との間の距離，dは線源と検出器面との間の直線距離（点(x_0,y_0,d)と点$(x_0,y_0,0)$の距離）である．

コリメータ応答関数を考慮したとき，画素$j(x_0,y_0,d)$から放出されたガンマ線が，検出器$i(x,y)$に検出される確率は，

$$a_{ij} = \frac{h(x,y,d)}{\sum_{i\in I} h(x,y,d)} \tag{4}$$

となる．ここでIは，検出器面に存在するすべての検出器である．検出確率を(4)式により導出し，画像再構成において検出確率として用いることにより，コリメータ開口補正を実装できる〔10,11〕．

3）吸収補正

式(5)に示すように吸収の影響を検出確率に組み込むことにより，吸収補正を行う．

$$a_{ij\_AC+} = a_{ij\_AC-}\cdot\exp\left(-\sum_{k\in L}\mu_k l\right) \tag{5}$$

ここでa_{ij_AC+}は吸収の影響を考慮した検出確率，a_{ij_AC-}は吸収の影響を考慮しない検出確率，Lはガンマ線が放出された画素jと検出器iの間の経路，μ_kは画素kにおける吸収係数[cm^{-1}]，lは，経路Lにおいて，画素kを通った距離である．

頭部は吸収係数分布の点から考えると，軟部組織と頭蓋骨の2つから成る単純な構造である．したがって，^{99m}Tcのエネルギーピーク140keVにおいては，2つの領域を考慮した均一な吸収係数0.167 cm^{-1}を頭部の輪郭内に設定したものを吸収係数マップとして画像再構成の検出確率に組み込むことで補正できる〔12〕．輪郭抽出は，しばしばSPECT投影データをフィルタ補正逆投影法（Filtered Back-Projection: FBP）で再構成した画像に対して，閾値処理して行われるが，本研究では大きさが既知のファントムを利用したので，閾値処理した輪郭の大きさがファントムと同じになるように，対話的に閾値を調整した．また，輪郭の多少のずれは再構成結果にあまり影響しない〔13〕．

4）モンテカルロ法に基づく散乱線補正

散乱線推定は，画像再構成により得た推定像